Comments are due by: Comments deadline

Measurement of angular and momentum distributions of charged particles within and around jets in Pb+Pb and pp collisions at $\sqrt{s_{\mathrm{NN}}} =$ 5.02 TeV with ATLAS at the LHC

Studies of the fragmentation of jets into charged particles in heavy-ion collisions can help in understanding the mechanism of jet quenching by the hot and dense QCD matter created in such collisions, the quark-gluon plasma. This paper presents a measurement of the angular distribution of charged particles around the jet axis in $\sqrt{s_{\mathrm{NN}}} =$ 5.02 TeV Pb+Pb and pp collisions, done using the ATLAS detector at the LHC. The measurement is performed for jets reconstructed with the anti-k_t algorithm with radius parameter $R = 0.4$, and is extended to a distance of $r = 0.8$ outside the jet cone. The charged particles in this analysis have transverse momenta in the 1 GeV–63 GeV range while jets have a transverse momenta in the 126 GeV–316 GeV range and are restricted to have an absolute value of the jet rapidity be less 1.7. Results are presented as a function of Pb+Pb collision centrality and distance from the jet axis for different jet and charged-particle transverse momenta ranges. There is an enhancement in the yields of charged particles with transverse momenta below 4 GeV in Pb+Pb collisions compared to pp collisions. This enhancement increases for larger angular distances from the jet axis, reaches a peak at $r = 0.6$ and decreases thereafter. Charged particles with transverse momenta above 4 GeV show a depletion in Pb+Pb collisions compared to the pp reference. An enhancement of charged particles of all transverse momenta is also observed in the jet core for distances up to $r = 0.05$ from the jet axis.

Measurement of angular and momentum distributions of charged particles within and around jets in Pb+Pb and pp collisions at $\sqrt{s_{\mathrm{NN}}} = 5.02$ TeV with ATLAS at the LHC

The ATLAS Collaboration

Studies of the fragmentation of jets into charged particles in heavy-ion collisions can help in understanding the mechanism of jet quenching by the hot and dense QCD matter created in such collisions, the quark-gluon plasma. This paper presents a measurement of the angular distribution of charged particles around the jet axis in $\sqrt{s_{\mathrm{NN}}} = 5.02$ TeV Pb+Pb and pp collisions, done using the ATLAS detector at the LHC. The measurement is performed for jets reconstructed with the anti-k_t algorithm with radius parameter $R = 0.4$, and is extended to a distance of $r = 0.8$ outside the jet cone. The charged particles in this analysis have transverse momenta in the 1 GeV–63 GeV range while jets have a transverse momenta in the 126 GeV–316 GeV range and are restricted to have an absolute value of the jet rapidity be less 1.7. Results are presented as a function of Pb+Pb collision centrality and distance from the jet axis for different jet and charged-particle transverse momenta ranges. There is an enhancement in the yields of charged particles with transverse momenta below 4 GeV in Pb+Pb collisions compared to pp collisions. This enhancement increases for larger angular distances from the jet axis, reaches a peak at $r = 0.6$ and decreases thereafter. Charged particles with transverse momenta above 4 GeV show a depletion in Pb+Pb collisions compared to the pp reference. An enhancement of charged particles of all transverse momenta is also observed in the jet core for distances up to $r = 0.05$ from the jet axis.

Contents

1 Introduction

Ultra-relativistic nuclear collisions at the Large Hadron Collider (LHC) produce hot, dense matter called the quark-gluon plasma, QGP (see Refs. [1, 2] for recent reviews). Hard-scattering processes occurring in these collisions produce jets which traverse and interact with the QGP. The comparison between the rates and the characteristics of these jets when produced in heavy-ion or pp collisions provides information on the properties of the QGP and how it interacts with partons from the hard scattering.

Jets with large transverse momenta are observed to be produced in central lead-lead (Pb+Pb) collisions at the LHC at a rate that is reduced by a factor of two with respect to the expectation from these cross sections measured in pp interactions, re-scaled by the nuclear overlap function of Pb+Pb collisions [3–6]. Similarly, back-to-back dijet [7–9] and photon-jet pairs [10] are observed to have unbalanced transverse momenta in Pb+Pb collisions compared to pp collisions. These observations suggest that some of the energy from the hard-scattered parton is transferred outside of the jet through its interaction with the QGP.

Also of interest are measurements sensitive to the distribution of particles within the jet. Measurements of the jet shape [11] and the longitudinal fragmentation functions [12–15] were performed in 2.76 TeV and 5.02 TeV Pb+Pb collisions. These measurements indicate that Pb+Pb collisions have an excess of low and high momentum particles along with a depletion of intermediate momentum particles inside the jet compared to pp collisions. Particles carrying a large fraction of the jet momentum are generally closely aligned with the jet axis, whereas low momentum particles can have a much broader angular distribution extending outside the jet [16, 17]. These observations suggest that the energy lost by jets as they propagate through the QGP, a process called jet-quenching, is being transferred to soft particles within and around the jet [18, 19]. Measurements of yields of these particles as a function of transverse momentum and angular

58 distance between the particle and the jet axis have a potential to provide additional constraints on models
59 of jet energy loss processes in Pb+Pb collisions.

60 This paper presents a measurement of charged particle p_{T} distributions inside and around jets. The
61 measured yields are defined as:

$$D(p_{\text{T}}, r) = \frac{1}{N_{\text{jet}}} \frac{1}{A} \frac{\mathrm{d}n_{\text{ch}}(p_{\text{T}}, r)}{\mathrm{d}p_{\text{T}}}, \tag{1}$$

62 where N_{jet} is the number of jets in consideration, $A = \pi(r_{\text{max}}^2 - r_{\text{min}}^2)$ is the area of an annulus around
63 the jet with its inner and outer radii r_{min} and r_{max}. The angular distance from the jet axis is given by
64 $r = \sqrt{\Delta\eta^2 + \Delta\phi^2}$ [1], and $n_{\text{ch}}(p_{\text{T}}, r)$ is the number of charged particles with a given p_{T} within the annulus.
65 The ratios of the charged-particle yields measured in Pb+Pb and pp collisions,

$$R_{D(p_{\text{T}}, r)} = \frac{D(p_{\text{T}}, r)_{\text{Pb+Pb}}}{D(p_{\text{T}}, r)_{pp}} \tag{2}$$

66 allow evaluation of modifications of the yields in Pb+Pb collisions compared to those in pp collisions. The
67 differences between the $D(p_{\text{T}}, r)$ distributions in Pb+Pb and pp collisions,

$$\Delta D(p_{\text{T}}, r) = D(p_{\text{T}}, r)_{\text{Pb+Pb}} - D(p_{\text{T}}, r)_{pp} \tag{3}$$

68 are also presented and allow for quantifying the absolute differences between the two collision systems
69 even in regions where the $D(p_{\text{T}}, r)$ distributions in pp tend toward 0.

70 The analysis is done using 0.49 nb^{-1} of Pb+Pb collisions and 25 pb^{-1} of pp collisions at center-of-mass
71 energy of 5.02 TeV collected in 2015 by ATLAS. Jets are reconstructed with the anti-k_t algorithm [20]
72 using a radius parameter $R = 0.4$ over a rapidity range of $|y^{\text{jet}}| < 1.7$. The measurement is presented for
73 jets with transverse momenta $p_{\text{T}}^{\text{jet}}$, in the 126–316 GeV range, for charged particles with $p_{\text{T}} > 1.0$ GeV and
74 for the following successive intervals in r around the jet, forming the annuli with inner and outer radii r_{min}
75 and r_{max}: 0.0, 0.05, 0.1, 0.15, 0.2, 0.25, 0.3, 0.4, 0.5, 0.6, 0.7, 0.8

2 Experimental setup

77 The measurements presented here are performed using the ATLAS calorimeter, inner detector, trigger,
78 and data acquisition systems [21]. The calorimeter system consists of a sampling liquid-argon (LAr)
79 electromagnetic (EM) calorimeter covering $|\eta| < 3.2$, a steel–scintillator sampling hadronic calorimeter
80 covering $|\eta| < 1.7$, LAr hadronic calorimeters covering $1.5 < |\eta| < 3.2$, and two LAr forward
81 calorimeters (FCal) covering $3.1 < |\eta| < 4.9$. The EM calorimeters are segmented longitudinally
82 in shower depth into three layers with an additional pre-sampler layer. They have segmentation that varies
83 with layer and pseudorapidity. The hadronic calorimeters have three sampling layers longitudinal in shower
84 depth.

---

[1] ATLAS uses a right-handed coordinate system with its origin at the nominal interaction point (IP) in the center of the detector, and the z-axis along the beam pipe. The x-axis points from the IP to the center of the LHC ring, and the y-axis points upward. Cylindrical coordinates (r, ϕ) are used the transverse plane, ϕ being the azimuthal angle around the z-axis. The pseudorapidity is defined in terms of the polar angle θ as $\eta = -\ln\tan(\theta/2)$. Transverse momentum and transverse energy are defined as $p_{\text{T}} = p\sin\theta$ and $E_{\text{T}} = E\sin\theta$, respectively. $\Delta R = \sqrt{(\Delta\eta)^2 + (\Delta\phi)^2}$ gives the angular distance between two objects with relative differences $\Delta\eta$ and $\Delta\phi$ in pseudorapidity and azimuth respectively.

The inner detector measures charged particles within the pseudorapidity interval $|\eta| < 2.5$ using a combination of silicon pixel detectors, silicon microstrip detectors (SCT), and a straw-tube transition radiation tracker (TRT), all immersed in a 2 T axial magnetic field [21]. Each of the three detectors is composed of a barrel and two symmetric end-cap sections. The pixel detector is composed of four layers including the "insertable B-layer" (IBL) [22, 23]. The SCT barrel section contains four layers of modules with sensors on both sides, and each end-cap consists of nine layers of double-sided modules with radial strips. The TRT contains layers of staggered straws interleaved with fibers in the barrel and end-cap.

The zero-degree calorimeters (ZDCs) are located symmetrically at $z = \pm 140$ m and cover $|\eta| > 8.3$. The ZDCs use tungsten plates as absorbers, and quartz rods sandwiched between the tungsten plates as the active medium. In Pb+Pb collisions the ZDCs primarily measure "spectator" neutrons, that is neutrons that do not interact hadronically when the incident nuclei collide. A ZDC coincidence trigger is implemented by requiring the pulse height from both ZDCs to be above a threshold to accept the single-neutron peak.

A two-level trigger system is used to select the Pb+Pb and pp collisions. The first level is based on custom electronics while the second level, the High Level Trigger (HLT), is based on software. Minimum-bias (MB) events are recorded using trigger defined by a logical OR of following two triggers: 1) total energy Level-1 trigger; 2) veto on the total energy trigger and ZDC coincidence trigger at Level-1 with the additional requirement of least one track in the HLT. The total-energy trigger required a total transverse energy measured in the calorimeter system to be greater than 50 GeV. Jet events are selected by the HLT, seeded by a jet identified by the Level-1 jet trigger in pp collisions or by the total-energy trigger with a threshold of 50 GeV in Pb+Pb collisions. The Level-1 jet trigger utilized in pp collisions required a jet with transverse momentum greater than 20 GeV. The HLT jet trigger used a jet reconstruction procedure similar to that used in the offline analysis as discussed in Section 4. It selected events containing jets with the transverse energy of at least 75 GeV in Pb+Pb collisions and at least 85 GeV in pp collisions. The measurement is performed in the jet transverse momentum range where the trigger is fully efficient.

3 Data sets and event selection

The Pb+Pb and pp data used in this analysis were recorded in 2015. The data samples consist of 25 pb^{-1} of $\sqrt{s}$ = 5.02 TeV pp and 0.49 nb^{-1} of $\sqrt{s_{NN}}$ = 5.02 TeV Pb+Pb data. In both samples, events are required to have a reconstructed vertex within 150 mm of the nominal interaction point along the beam axis. Only events taken during stable beam conditions and satisfying detector and data-quality requirements that include the calorimeters and inner tracking detectors being in nominal operating conditions are considered.

In Pb+Pb collisions, the event centrality reflects the overlap area of the two colliding nuclei and is characterized by $\Sigma E_{\mathrm{T}}^{\mathrm{FCal}}$, the total transverse energy deposited in the FCal [24]. The six centrality intervals used in this analysis are defined according to successive percentiles of the $\Sigma E_{\mathrm{T}}^{\mathrm{FCal}}$ distribution obtained in minimum-bias collisions, ordered from the most central (highest $\Sigma E_{\mathrm{T}}^{\mathrm{FCal}}$) to the most peripheral (lowest $\Sigma E_{\mathrm{T}}^{\mathrm{FCal}}$) collisions: 0–10%, 10–20%, 20–30%, 30–40%, 40–60%, 60–80%.

In addition to the jet-triggered sample, a separate minimum bias Pb+Pb data sample was recorded with three trigger selections: the minimum-bias trigger and two total transverse-energy triggers with thresholds of 1.5 TeV and 6.5 TeV used to enhance the rate of central Pb+Pb events. This sample is combined with a set of 1.8×10^7 5.02 TeV hard-scattering dijet pp events generated with Powheg+Pythia8 [25, 26] using the A14 tune of parameters [27] and the NNPDF23LO PDF set [28] to produce the Monte Carlo Overlay

sample. This sample is reweighed on an event by event basis such it has the same centrality distribution as the jet triggered sample. A separate set of 1.8×10^7 5.02 TeV hard-scattering dijet pp events generated with the same tune and PDFs was used as the pp MC. The detector response is simulated in both MC samples using Geant4 [29, 30] and they are then used to evaluate the performance of the detector and analysis procedure. Another sample of minimum bias Pb+Pb events is generated using HIJING (version 1.38b) [30] and is used to evaluate the track reconstruction performance.

4 Jet and track selection

The jet reconstruction procedure is identical to [6]. The anti-k_t algorithm is first run in four-momentum recombination mode, on $\Delta\eta \times \Delta\phi = 0.1 \times 0.1$ calorimeter towers with two anti-k_t distance parameter values ($R = 0.2$ and $R = 0.4$). The energies in the towers are obtained by summing the energies of calorimeter cells at the electromagnetic energy scale within the tower boundaries. Then, an iterative procedure is used to estimate the η-dependent underlying event (UE) transverse energy density, while excluding the regions populated by jets. The estimate of the UE contribution is performed on an event-by-event basis. Furthermore, the background is modulated to account for the presence of the azimuthal anisotropy of particle production [31]. The modulation accounts for the contribution of the second, third, and fourth order azimuthal anisotropy harmonics. The UE transverse energy is subtracted from calorimeter towers included in the jet and the four-momentum of the jet is updated accordingly. Then, a jet η- and p_T-dependent correction factor to the p_T^{jet} derived from the simulation samples is applied to correct for the calorimeter energy response [32]. The same calibration factors are applied both in pp and Pb+Pb collisions. An additional correction based on *in-situ* studies of jets recoiling against photons, Z bosons, and jets in other regions of the calorimeter is applied [33, 34]. The same jet reconstruction procedure without the azimuthal modulation of the UE is also applied to pp collisions. In this analysis, jets are required to have p_T^{jet} in the 126–316 GeV range, with rapidity $|y^{\text{jet}}| < 1.7$. To prevent nearby jets from distorting the measurement of $D(p_T, r)$ distributions, jets are rejected if there is another jet with a higher p_T^{jet} than the considered jet anywhere within an angular distance of $\Delta R < 1.0$. The isolation requirement removes approximately 0.01% of jets, and has a negligible impact on the final measurement.

Charged-particle tracks in Pb+Pb collisions are reconstructed from hits in the inner detector using the track reconstruction algorithm with settings optimized for the high hit density in heavy-ion collisions [35]. Tracks used in this analysis are required to have at least 9 (11) total silicon hits for charged particles with pseudorapidity, $|\eta^{\text{ch}}| \leq 1.65$ ($|\eta^{\text{ch}}| > 1.65$). At least one hit is required in one of the two innermost pixel layers. If the track trajectory passes through an active module in the innermost layer, then a hit in this layer is required. Additionally, a track must have no more than two holes in the pixel and SCT detectors together, where a hole is defined by the absence of a hit predicted by the track trajectory. All charged-particle tracks used in this analysis are required to have reconstructed transverse momentum $p_T^{\text{ch}} > 1.0$ GeV. In order to suppress a contribution from secondary particles, the distance of closest approach of the track to the primary vertex is required to be less than a value which varies from 0.45 mm at $p_T^{\text{ch}} = 4$ GeV to 0.2 mm at $p_T^{\text{ch}} = 20$ GeV in the transverse plane and less than 1.0 mm in the longitudinal direction.

The efficiency, ε, for reconstructing charged particles in Pb+Pb and pp collisions is evaluated as a function of the generator-level primary particle[2] transverse momentum, p_T^{truth}, and pseudorapidity, η^{truth}, by associating tracks to generator-level primary particles using the MC samples described above [30].

---

[2] Primary particles are defined as particles with a mean lifetime $\tau > 0.3 \times 10^{-10}$s either directly produced in pp interactions or from subsequent decays of particles with a shorter lifetime. All other particles are considered to be secondary.

166 For Pb+Pb collisions the efficiency is also evaluated separately in each centrality interval used in the
167 measurement. In both collision systems the efficiency increases slowly with p_T^{truth} and is seen to be
168 independent of p_T^{jet} in the measurement phase space. It is approximately 0.8 at $p_T = 1$ GeV and rises to
169 approximately 0.9 at $p_T = 63$ GeV. The variation in efficiency between the most central and peripheral
170 Pb+Pb collisions is approximately 3%.

171 The contribution of reconstructed tracks that cannot be matched to a generated primary particle in the pp
172 MC samples, along with the residual contribution of tracks matched to secondary particles, are together
173 called the contribution from "fake" tracks. This contribution is less than 2% in the entire p_T^{ch} range under
174 study in both pp and Pb+Pb collisions.

5 Analysis procedure

176 The analysis procedure is similar to the procedure in [15] with the additional requirement of being done
177 differentially in r. Measured tracks are associated with a reconstructed jet if they fall within $\Delta R < 0.8$ of
178 the jet axis and are constructed as:

$$\frac{\mathrm{d}^2 n_{ch}^{meas}}{\mathrm{d}p_T^{ch}\mathrm{d}r} = \frac{1}{\varepsilon(p_T^{ch}, \eta^{ch})} \frac{\Delta n_{ch}(p_T^{ch}, r)}{\Delta p_T^{ch}\Delta r} \tag{4}$$

179 where $\Delta n_{ch}(p_T^{ch}, r)$ represents the number of tracks within a given p_T^{ch} and r range. The efficiency correction
180 is applied as a $1/\varepsilon(p_T^{ch}, \eta^{ch})$ weight on a track-by-track basis, assuming $p_T^{ch} = p_T^{truth}$. While that assumption
181 is not strictly valid, the efficiency varies sufficiently slowly with p_T^{truth} that the error introduced by this
182 assumption is less than 1%.

183 The measured track yields need to be corrected for the underlying event and fakes from the soft processes.
184 In pp collisions, the UE contribution is negligible due to minimal pileup and the fake subtraction is done
185 by estimating fake rates from the MC samples using tracks that do not have an associated truth match. For
186 Pb+Pb collisions, the fakes and UE are estimated together in a two step process: first, MC overlay events
187 reweighed to match the centrality distribution in jet triggered data are used to generate $\eta - \phi$ maps of the
188 average number of particles in a given annulus around a jet. This is done for tracks without a truth match
189 and as a function of p_T^{jet}, η^{jet}, ϕ^{jet}, angle of the jet to the reaction plane[3] $\mathrm{d}\Psi_{jet}$, r, p_T, and centrality. In the
190 second step, the $\eta - \phi$ maps are convoluted with η_{jet}, ϕ_{jet}, and $\mathrm{d}\Psi_{jet}$ distributions in the jet triggered data to
191 estimate the yields of charged particles for the jet under study, $\mathrm{d}^2 n_{ch}^{UE+Fake}(r)/\mathrm{d}p_T^{ch}\mathrm{d}r|_{cent}$. The yields are
192 independent of the angular distance r, decrease with the decreasing collision centrality, increasing p_T^{ch}, and
193 increasing azimuthal distance to the second-order event plane.

$$\frac{\mathrm{d}^2 n_{ch}^{sub}}{\mathrm{d}p_T^{ch}\mathrm{d}r} = \frac{\mathrm{d}^2 n_{ch}^{meas}}{\mathrm{d}p_T^{ch}\mathrm{d}r} - \frac{\mathrm{d}^2 n_{ch}^{UE+Fake}(r)}{\mathrm{d}p_T^{ch}\mathrm{d}r} \tag{5}$$

---

[3] The reaction plane angle Ψ is determined on an event-by-event basis by a standard method using the ϕ variation of transverse energy in the forward calorimeter [31]
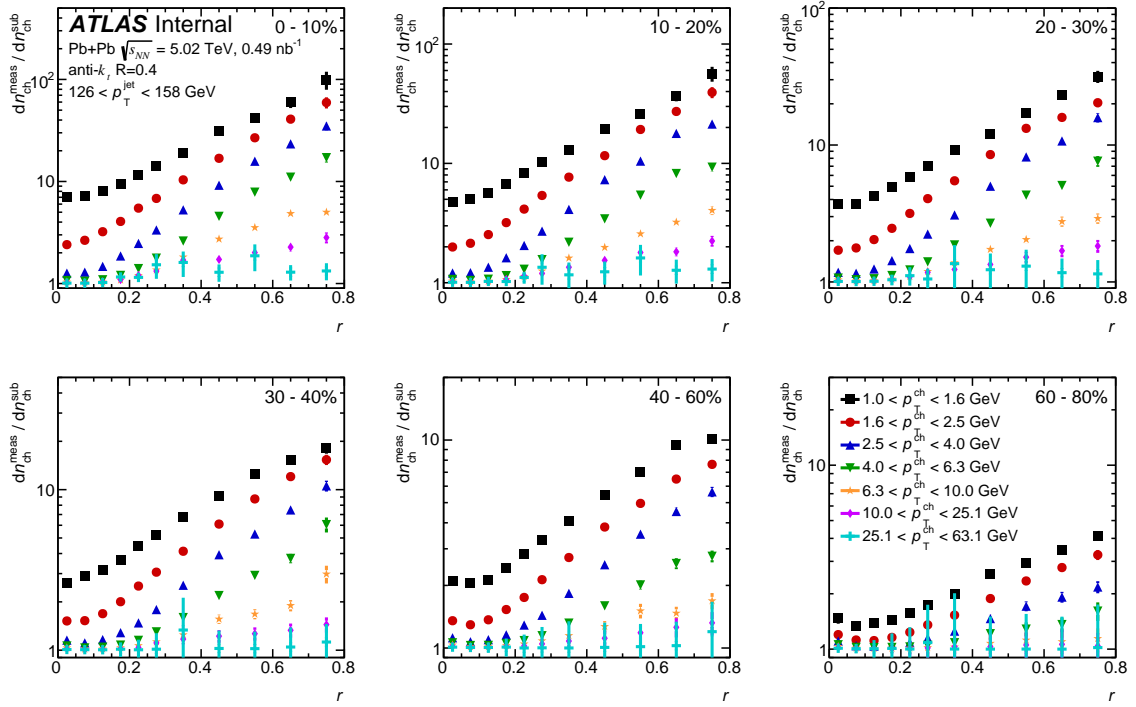
Figure 1: Ratio of the raw charged particle distributions to those after the subtraction of the UE and fake tracks as a function of r for different p_T^{ch} intervals, six centrality selections and for p_T^{jet} between 126–158 GeV.

Figure 1 shows the charged-particle distributions prior to the UE and fake track subtraction, $d^2 n_{ch}^{meas}/dp_T^{ch}dr$, divided by the distributions after the subtraction, $d^2 n_{ch}^{sub}/dp_T^{ch}dr$ as a function of r for different p_T^{ch} intervals and $126 < p_T^{jet} < 158$ GeV for six centrality selections. The UE is the highest for 1.0 GeV charged particles at large values of r and in central collisions for p_T^{jet} between 126–158 GeV, with the signal to background being approximately 1:100. It is rapidly decreasing towards more peripheral collisions, larger p_T^{ch} and smaller r. Furthermore, the ratio slowly decreases with increasing p_T^{jet}.

The intrinsic underlying event from the hard scattering process is not subtracted in both pp and Pb+Pb collisions because this would be generator dependent and make comparisons between the two systems non-trivial.

To remove the effects of the bin migration due to the jet energy and track-momentum resolution, the subtracted $d^2 n_{ch}^{sub}/dp_T^{ch}dr$ distributions are corrected by a two-dimensional Bayesian unfolding [36] in p_T^{ch} and p_T^{jet} as implemented in the RooUnfold package [37]. Two-dimensional unfolding is used because the calorimetric jet energy response depends on the fragmentation pattern of the jet [38]. Four-dimensional response matrices are created from the pp and Pb+Pb MC samples using the generator-level and reconstructed p_T^{jet}, and the generator-level and reconstructed charged-particle p_T^{ch}. They are corrected for tracking efficiencies and are evaluated in bins of r and centrality. The Bayesian procedure requires a choice in the number of iterations. Additional iterations reduce the sensitivity to the choice of prior, but may amplify statistical fluctuations in the distributions. After four iterations the charged particle distributions are found to be stable for both the Pb+Pb and pp data. A separate one-dimensional Bayesian unfolding is used to correct the measured p_T^{jet} spectra that are used to normalize the unfolded charged particle distributions. To achieve

214 better correspondence with the data, the response matrices for both the one and two dimensional unfolding
215 are reweighed so that the distributions match the shapes in the reconstructed data.

216 An independent bin-by-bin unfolding procedure is also used to correct for migrations originating from the
217 finite jet and track angular resolutions. Two corresponding $D(p_T, r)$ distributions are evaluated in MC
218 samples, one using generator-level jets and primary particles and the other using reconstructed jets and
219 charged particles with their reconstructed p_T^{ch} replaced by generator-level transverse momentum, p_T^{truth}. The
220 ratio of these two MC distributions provides a correction factor which is then applied to the data.

221 The final particle-level corrected distributions, normalized by the area of the annulus under question are
222 defined as:

$$D(p_T, r) = \frac{1}{N_{jet}^{unfolded}} \frac{1}{A(r)} \frac{d^2 n_{ch}^{unfolded}(r)}{dp_T dr}, \qquad (6)$$

223 where $N_{jet}^{unfolded}$ is the unfolded number of jets in a given p_T^{jet} interval.

224 The performance of the full analysis procedure is validated in the MC samples by comparing the fully
225 corrected charged particle distributions to the generator-level distributions. Good closure ($< 3\%$) is seen
226 for low p_T particles. Algorithmic effects from the jet reconstruction software in reconstructing high p_T
227 particles near the jet edge lead to a larger non-closure in those regions of the measurement phase-space.
228 The analysis is done where the non-closure in the pp MC sample is less than 5%, excluding the following
229 regions of phase space: 6–10 GeV tracks above $r > 0.3$, 10–25 GeV tracks above $r > 0.3$, and 25–63 GeV
230 tracks above $r > 0.2$ for 126–158 GeV jets; 10–25 GeV tracks above $r > 0.4$, and 25–63 GeV tracks above
231 $r > 0.3$ for 158–200 GeV jets; 25–63 GeV tracks above $r > 0.3$ for 200–251 GeV jets.

6 Systematic uncertainties

233 The following sources of systematic uncertainty are considered: the jet energy scale (JES), the jet energy
234 resolution (JER), the sensitivity of the unfolding to the prior, the UE contribution, the residual non-closure
235 of the analysis procedure, and tracking-related uncertainties. For each systematic variation, the $D(p_T, r)$
236 distributions along with their ratios and differences are re-evaluated. The difference between the varied and
237 nominal distributions is used as an estimate of the uncertainty.

238 The systematic uncertainty due to the JES in Pb+Pb collisions is composed of two parts: a centrality-
239 independent baseline component and a centrality-dependent component. Only the centrality-independent
240 baseline component is used in pp collisions; it is determined from *in-situ* studies of the calorimeter
241 response [32, 38, 39] and the relative energy scale difference between the jet reconstruction procedure in
242 heavy-ion collisions [39] and the procedure used in pp collisions [40]. The centrality-dependent uncertainty
243 reflects a modification of parton showers by the Pb+Pb environment. It is evaluated by comparing
244 calorimeter p_T^{jet} and the sum of the transverse momentum of tracks within the jet in data and MC. The
245 size of the centrality-dependent uncertainty on the JES reaches 0.5% in the most central collisions. Each
246 component that contributes to the JES uncertainty is varied separately by ±1 standard deviation for each
247 interval in p_T^{jet} and the response matrix is recomputed accordingly. The data are unfolded with modified
248 matrices. The resulting uncertainty from the JES increases with increasing charged-particle p_T at fixed p_T^{jet}
249 and decreases with increasing p_T^{jet}, and is at the level of 2–4%.

The uncertainty on the $D(p_T, r)$ distributions due to the JER is evaluated by repeating the unfolding procedure with modified response matrices, where an additional contribution is added to the resolution of the reconstructed p_T^{jet} using a Gaussian smearing procedure. The smearing factor is evaluated using an *in-situ* technique in 13 TeV pp data involving studies of dijet energy balance [41, 42]. An additional uncertainty is included to account for differences between the tower-based jet reconstruction and that used in analyses of 13 TeV pp data. The resulting uncertainty from the JER is symmetrized to account for negative variations of the JER. The size of the resulting uncertainty on the $D(p_T, r)$ distributions due to the JER typically reaches 4–5% for the highest charged-particle p_T intervals and decreases to 2–3% with decreasing charged-particle p_T at fixed p_T^{jet}.

The uncertainties related to track reconstruction and selection originate from several sources. Uncertainties related to the material description in simulation and the track transverse momentum resolution are obtained from studies in data and simulation described in Ref. [43]. The sensitivity of the tracking efficiency to the description of the inactive material in the MC samples is evaluated by varying the material description. This resulting uncertainty in the track reconstruction efficiency is between 0.5% and 2% in the track p_T range used in the analysis. The systematic uncertainty on the fake track rate is 30% in both collision systems [43]. The contamination of fake tracks is less than 2% and the resulting uncertainty in the $D(p_T, r)$ distributions is at most 5%. An additional uncertainty takes into account a possible residual misalignment of the tracking detectors in pp and Pb+Pb data-taking. The alignment in these datasets is checked *in-situ* with $Z \rightarrow \mu^+\mu^-$ events, and thus a track-p_T dependent uncertainty arises from the finite size of this sample. The resulting uncertainties in the $D(p_T, r)$ distributions are typically less than 0.1%. An additional uncertainty in the tracking efficiency due to the high local track density in the core of jets is 0.4% [44] for all p_T^{jet} ranges in this analysis. The uncertainty due to the track selection is evaluated by repeating the analysis with an additional requirement on the significance of the distance of closest approach of the track to the primary vertex. This uncertainty affects the track reconstruction efficiencies, track momentum resolution, and rate of fake tracks. The resulting uncertainty typically varies between 1–2%. Finally, the track-to-particle association requirements are varied. This variation affects the track reconstruction efficiency, track momentum resolution, and rate of fake tracks. The resulting systematic uncertainty is $\leq 0.1\%$ on the $D(p_T, r)$ distributions. All track-related systematic uncertainties are added in quadrature and presented as total tracking uncertainty.

The systematic uncertainty associated with the UE subtraction has two components: limited statistics of charged particles associated with a jet without a corresponding generator particle in the Pb+Pb MC, and a comparison to an alternative UE estimation done using the cone method (described in detail in [14, 15]). The cone method uses jet triggered events to estimate the background and is adapted from [15]. A regular grid of 9 cones of size $R = 0.8$ is used to cover the full inner detector region. Cones are excluded if they are within an angular distance of $dR = 1.6$ to a reconstructed jet with $p_T^{jet} > 90$ GeV or if they contain a track with $p_T > 10$ GeV. This exclusion removes biases from any hard processes. The resulting UE charged particle yields $dn_{ch}^{UE \, Cone}/dp_T^{ch}$ are evaluated over the 1–10 GeV range as a function of p_T, p_T^{jet}, centrality, and r, and are subsequently averaged over all cones. The UE uncertainty on the $D(p_T, r)$ distributions is approximately 40% at the largest angular distances from the jet axis and rapidly decreases with increasing charged-particle p_T and decreasing distance. This is the dominant source of the systematic uncertainty at low charged-particle p_T and large r.

The systematic uncertainty on the unfolding procedure is estimated by generating the response matrices from the MC distributions without any re-weighting to match shapes in data. Conservatively, the difference between the nominal $D(p_T, r)$ distribution and $D(p_T, r)$ unfolded with the re-weighted response matrices is taken as the systematic uncertainty, and is at the level of 5–7%.

295 Conservatively, an additional uncertainty to account for possible residual limitations in the analysis
296 procedure is assigned by evaluating the non-closure of the unfolded distributions in simulations. This is
297 typically at the level of 3-4% and is described in Section 5.

298 The correlations between the various systematic components are considered in evaluating the $R_{D(p_T,r)}$ and
299 $\Delta D(p_T, r)$ distributions. The unfolding and non-closure uncertainty are taken to be uncorrelated between
300 pp and Pb+Pb collisions, while all other uncertainties are taken to be correlated. For these, the $R_{D(p_T,r)}$ and
301 $\Delta D(p_T, r)$ distributions are re-evaluated by applying the variation to both collision systems; the resulting
302 variations of the ratios from their central values are used as the correlated systematic uncertainty.

303 Examples of systematic uncertainties in the $D(p_T, r)$ distributions for jets in the 126–158 GeV p_T^{jet} range
304 measured in pp and Pb+Pb collision systems are shown in Figure 2. The uncertainties on the $R_{D(p_T,r)}$
305 distributions are shown in Figure 3. It can be seen that the dominant systematic uncertainty on the Pb+Pb
306 and the $R_{D(p_T,r)}$ distributions is from the underlying event estimation. While it is less than 5% for $r < 0.3$
307 from the jet axis, it is approximately 40% at for 1 GeV tracks at $r = 0.8$ from the jet axis. The uncertainties
308 in the pp system are smaller, with the dominant systematic uncertainty coming from the tracking. This
309 uncertainty is approximately 10% for $r < 0.1$ and decreases to less than 5% at larger distances.

7 Results

311 The $D(p_T, r)$ distributions are studied as a function of p_T^{jet} for pp data and Pb+Pb collisions with different
312 centralities. Ratios and differences between $D(p_T, r)$ distributions in Pb+Pb and pp collisions are evaluated
313 to explore the interplay between the hot and dense matter and the parton shower.

314 The $D(p_T, r)$ distributions evaluated in pp and Pb+Pb collisions for $126 < p_T^{\text{jet}} < 158$ GeV are shown
315 in Figure 4. The distributions exhibit a difference in shape between Pb+Pb and the pp reference, with
316 the Pb+Pb distributions being broader at low p_T ($p_T < 4$ GeV) and narrower at high p_T ($p_T > 4$ GeV) in
317 0–10% central collisions. This modification is centrality dependent and is smaller for peripheral Pb+Pb
318 collisions.

319 Ratios of the $D(p_T, r)$ distributions in Pb+Pb to those measured in pp for $126 < p_T^{\text{jet}} < 158$ GeV and
320 $200 < p_T^{\text{jet}} < 251$ GeV jets and are presented in Figure 5. They are shown as a function of r for
321 different p_T and centrality selections. In 0–10% central collisions, $R_{D(p_T,r)}$ is above unity for $r < 0.7$ for
322 charged-particles with p_T less than 4 GeV in both jet selections. For these particles, the enhancement
323 of the charged particle spectra grows with increasing r up to $r = 0.3$. It is approximately constant over
324 $0.3 – 0.6$ and decreases for $r > 0.6$. For charged particles with $p_T > 4.0$ GeV, $R_{D(p_T,r)}$ shows a depletion
325 outside the jet core for $r > 0.05$. The magnitude of this depletion increases with increasing r up to $r = 0.3$
326 and is approximately constant thereafter. The observed behavior inside the jet ($r < 0.4$) agrees with the
327 measurement of the inclusive jet fragmentation functions [9, 15], where yields of fragments with $p_T < 4$
328 GeV are observed to be enhanced and yields of charged particles with intermediate p_T are suppressed
329 in Pb+Pb collisions compared to those in pp for collisions. For peripheral collisions, $R_{D(p_T,r)}$ has no
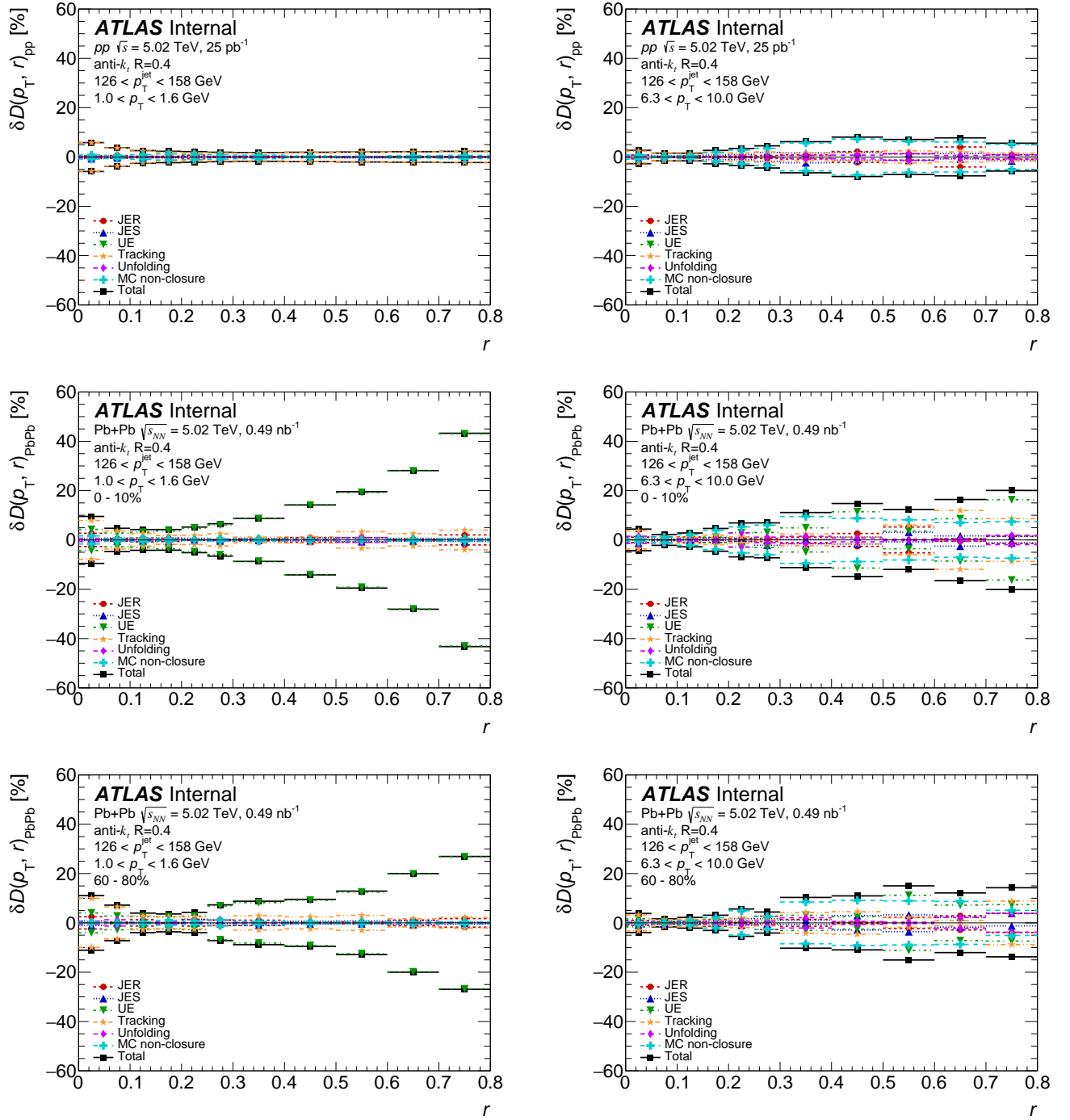330 significant r dependence and the distributions do not significantly deviate from unity.

Figure 2: Relative size of the systematic uncertainties for $D(p_T, r)$ distributions in pp (top), central 0–10% Pb+Pb (middle), and peripheral 60–80% Pb+Pb (bottom) collisions for tracks with $1.0 < p_T < 1.6$ GeV (left) and $6.3 < p_T < 10$ GeV (right) in jets with $126 < p_T^{jet} < 158$ GeV. The systematic uncertainties due to JES, JER, unfolding, UE contribution, MC non-closure, and tracking are shown along with the total systematic uncertainty from all sources.
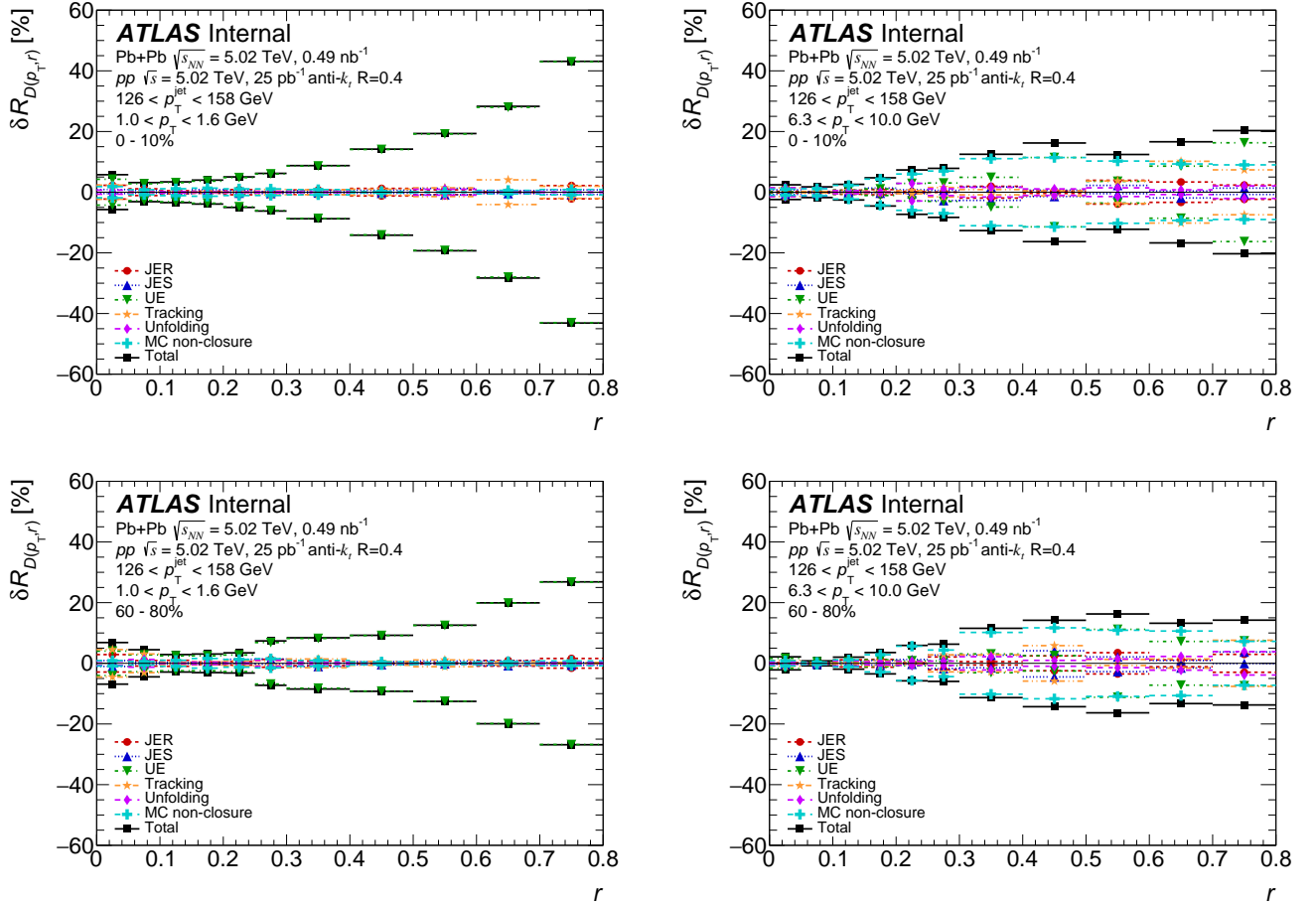
Figure 3: Relative size of the systematic uncertainties for $R_{D(p_T, r)}$ distributions for 0–10% (top) and 60–80% (bottom) Pb+Pb collisions, for tracks with $1.0 < p_T < 1.6$ GeV (left) and $6.3 < p_T < 10.0$ GeV (right), in jets with $126 < p_T^{jet} < 158$ GeV. The systematic uncertainties due to JES, JER, unfolding, UE contribution, MC non-closure, and tracking are shown along with the total systematic uncertainty from all sources.
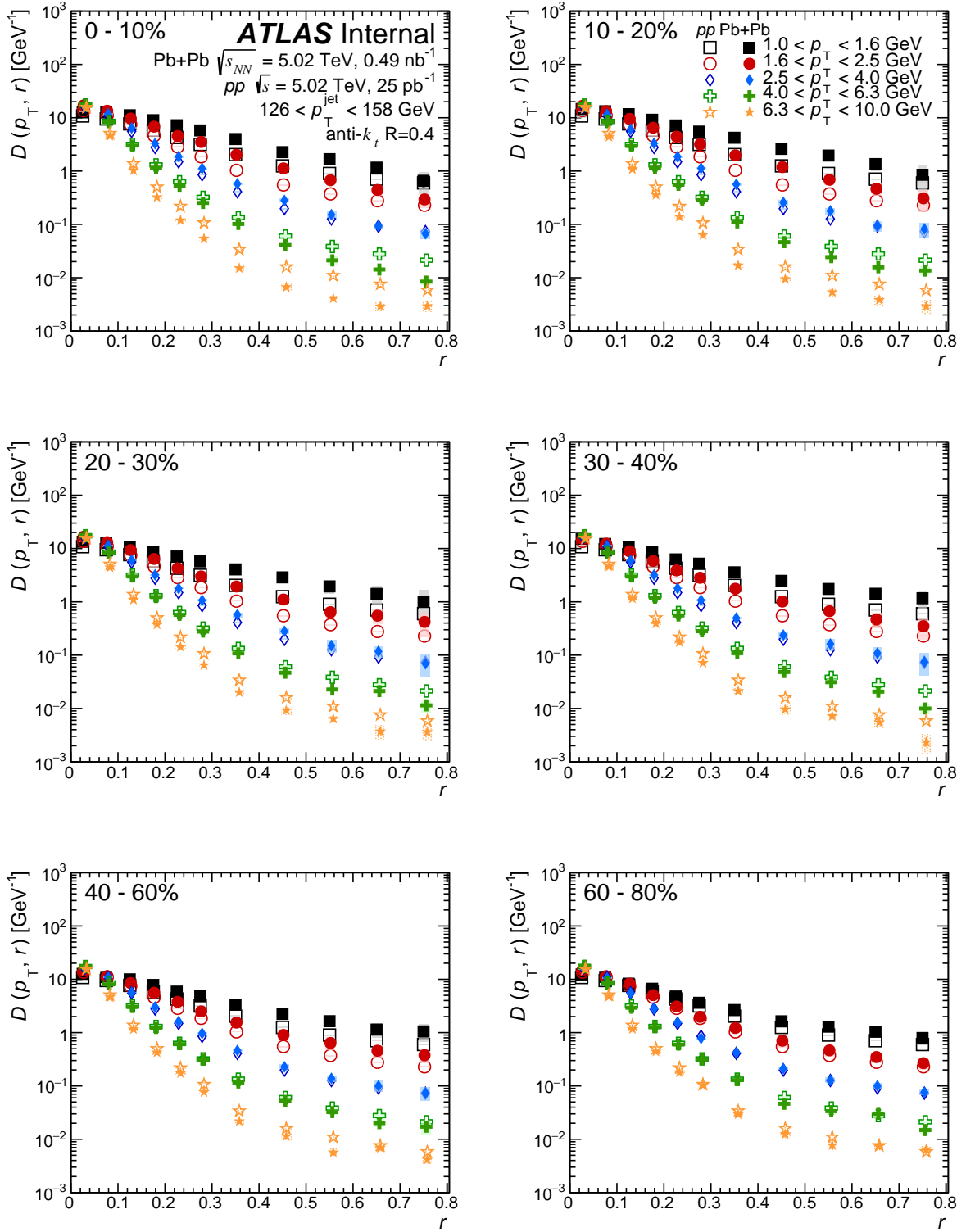
Figure 4: The $D(p_T, r)$ distributions in pp (open symbols) and Pb+Pb (closed symbols) as a function of angular distance r for p_T^{jet} of 126 to 158 GeV. The colors represent different track p_T ranges, and each panel is a different centrality selection. The vertical bars on the data points indicate statistical uncertainties while the shaded boxes indicate systematic uncertainties. The widths of the boxes are not indicative of the bin size and the points are shifted horizontally for better visibility.
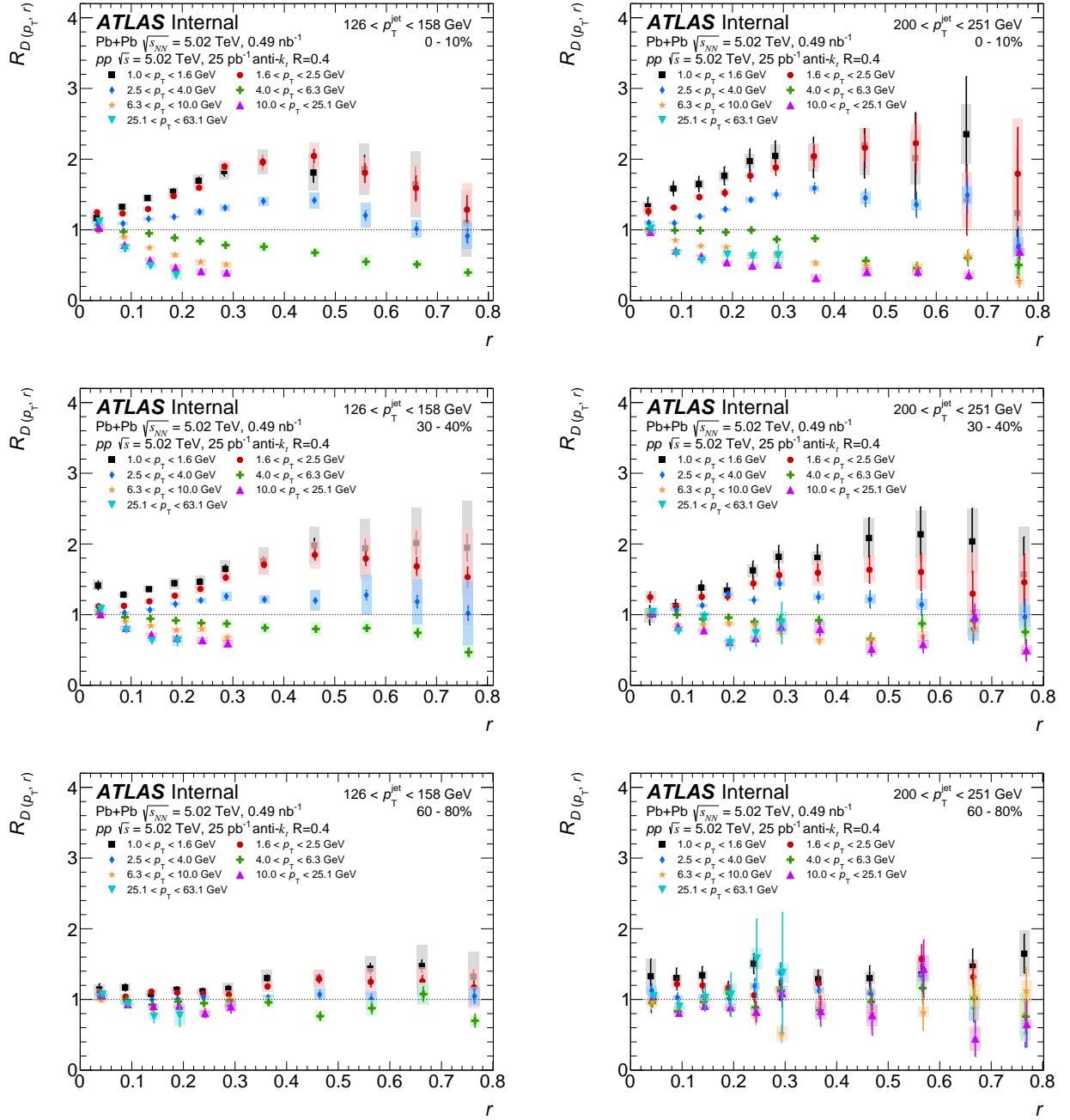
Figure 5: Ratios of $D(p_T, r)$ distributions in 0–10% (top), 30–40% (middle), and 60–80% (bottom) Pb+Pb collisions to pp collisions as a function of angular distance r for p_T^{jet} of 126 to 158 GeV (left) and of 200 to 251 GeV (right) for six p_T selections. The vertical bars on the data points indicate statistical uncertainties while the shaded boxes indicate systematic uncertainties. The widths of the boxes are not indicative of the bin size and the points are shifted horizontally for better visibility.

8 Discussion

This section discusses the results from the previous section.

The centrality dependence of $R_{D(p_T,r)}$ for two charged-particle p_T intervals: 1.0–1.6 GeV and 6.3–10.0 GeV, and two different p_T^{jet} ranges: 126–158 GeV and 200–251 GeV, is presented in Figure 6. The magnitude of these modifications decreases for more peripheral collisions and $R_{D(p_T,r)}$ approaches unity in 60–80% central collisions for both p_T ranges, across the entire $r < 0.8$ range under investigation. It can also be seen that the higher p_T^{jet} range shows a larger modification in central collisions.
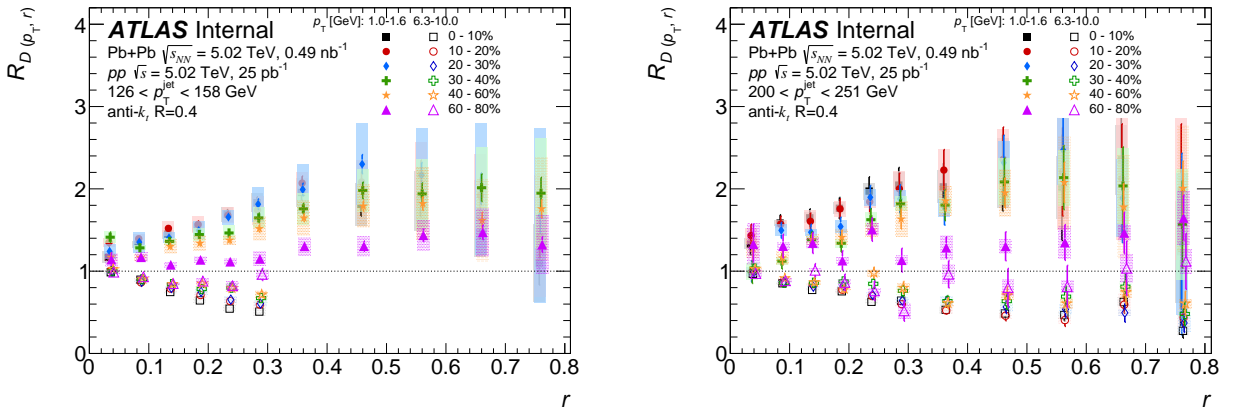
Figure 6: The $R_{D(p_T,r)}$ distributions for p_T^{jet} of 126–158 GeV and 200–251 GeV as a function of angular distance r for two p_T selections and six centrality intervals (p_T selections are shown by closed and open symbols). The vertical bars on the data points indicate statistical uncertainties while the shaded boxes indicate systematic uncertainties. The widths of the boxes are not indicative of the bin size and the points are shifted horizontally for better visibility.

The p_T^{jet} dependence of $R_{D(p_T,r)}$ for two p_T intervals: 1.0–1.6 GeV and 6.3–10.0 GeV, in 0–10% central Pb+Pb collisions is presented in Figure 7. A trend of increasing $R_{D(p_T,r)}$ with increasing p_T^{jet} is observed for $0.0 < r < 0.25$ for low pt particles. The higher-p_T charged particles have $R_{D(p_T,r)}$ values that decrease with increasing r; no significant dependence on p_T^{jet} is observed.

The charged particle p_T dependence of $R_{D(p_T,r)}$ for $126 < p_T^{\text{jet}} < 158$ GeV and $200 < p_T^{\text{jet}} < 251$ GeV, at a variety of angular distances from the jet axis in 0–10% central and 60–80% peripheral collisions is presented in Figure 8. No suppression is observed for $r < 0.05$ across the entire p_T range under investigation. This can also be seen in Figure 5 and Figure 9, where any suppression in the charged particle spectra is at distances larger than $r = 0.05$ from the jet axis.

Differences between the $D(p_T,r)$ distributions in Pb+Pb and pp, given as:

$$\Delta D(p_T,r) = D(p_T,r)_{\text{Pb+Pb}} - D(p_T,r)_{pp} \tag{7}$$

are presented as a function of r for different p_T selections in 0–10% central collisions in Figure 11. These distributions indicate an excess (depletion) in the charged-particle yield density for Pb+Pb collisions compared to pp collisions for charged particles with low (high) p_T. This excess ranges from 0.5 to 4
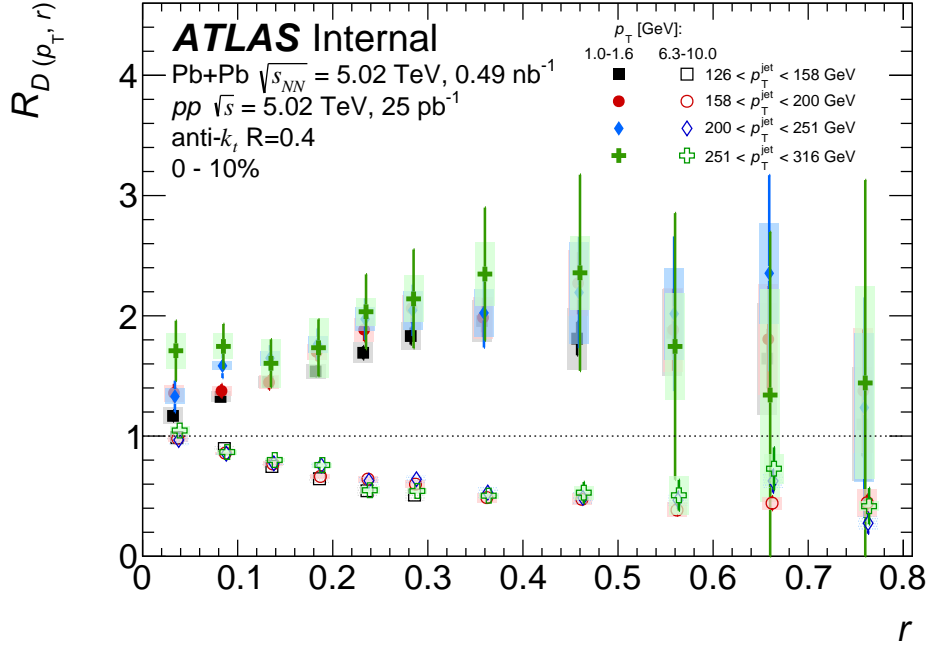
Figure 7: $R_{D(p_T, r)}$ as a function of r for 0–10% collisions for charged particles with $1.0 < p_T < 1.6$ GeV (closed symbols) and $6.3 < p_T < 10.0$ GeV (open symbols) for different p_T^{jet} selections. The vertical bars on the data points indicate statistical uncertainties while the shaded boxes indicate systematic uncertainties. The widths of the boxes are not indicative of the bin size and the points are shifted horizontally for better visibility.

particles per unit area at 1 GeV in 126–158 GeV jets for 0–10% central Pb+Pb collisions and increases with increasing p_T^{jet}. The depletion for high p_T particles is at most 0.5 particles per unit area for 126–158 GeV jets in 0–10% central Pb+Pb collisions and increases for higher p_T^{jet}. There is a minima in the $\Delta D(p_T, r)$ distribution for charged particles with $p_T > 4$ GeV at $0.05 < r < 0.10$ that is seen at all p_T^{jet} ranges under investigation.

The $D(p_T, r)$ distribution can be integrated for particles with $p_T < 4$ GeV to construct the quantities Θ and P.

$$\Theta_x = \int_1^4 D(p_T, r)|_x \tag{8}$$

$$P_x = \int_0^r \int_1^4 D(p_T, r) \mathrm{d}p_T \mathrm{d}r'|_x \tag{9}$$

where $x \in [pp, \text{Pb+Pb}]$. These can be compared between the pp and Pb+Pb systems to give the following distributions:

$$\Delta_\Theta = \Theta_{\text{Pb+Pb}} - \Theta_{pp} \qquad \Delta_P = P_{\text{Pb+Pb}} - P_{pp} \tag{10}$$

$$R_\Theta = \frac{\Theta_{\text{Pb+Pb}}}{\Theta_{\text{Pb+Pb}}} \qquad R_P = \frac{P_{\text{Pb+Pb}}}{P_{pp}} \tag{11}$$

These variables provide aggregate information for particles with $p_T < 4$ GeV, both differentially and cumulatively in r.
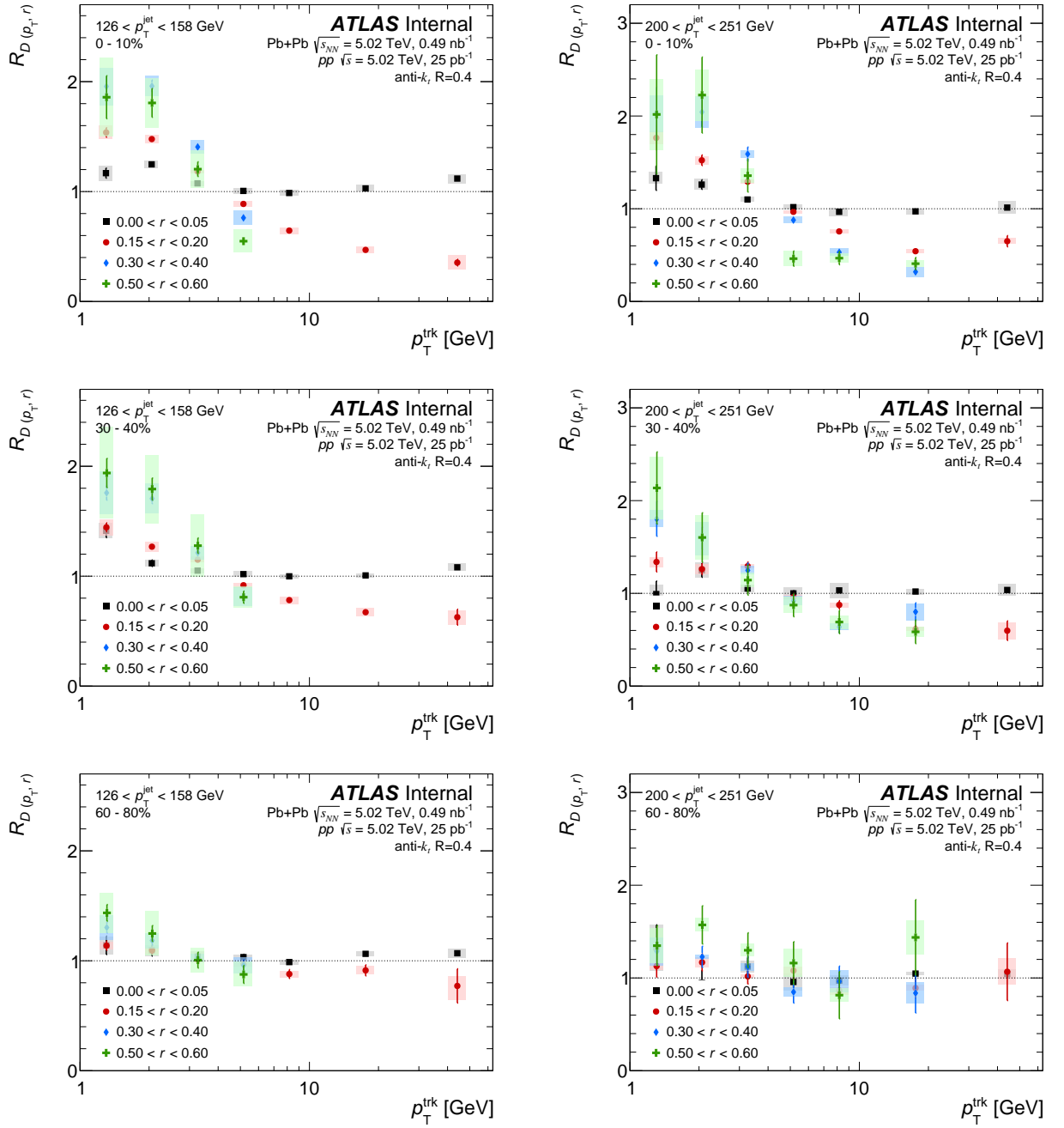
Figure 8: $R_{D(p_T,r)}$ as a function of p_T in 0–10% (top), 30–40% (middle), and 60–80% (bottom) Pb+Pb collisions to pp collisions for two different p_T^{jet} selections: 126–158 GeV (left) and 200–251 GeV (right). The different colors indicate different angular distances from the jet axis. The vertical bars on the data points indicate statistical uncertainties while the shaded boxes indicate systematic uncertainties. The widths of the boxes are not indicative of the bin size and the points are shifted horizontally for better visibility.
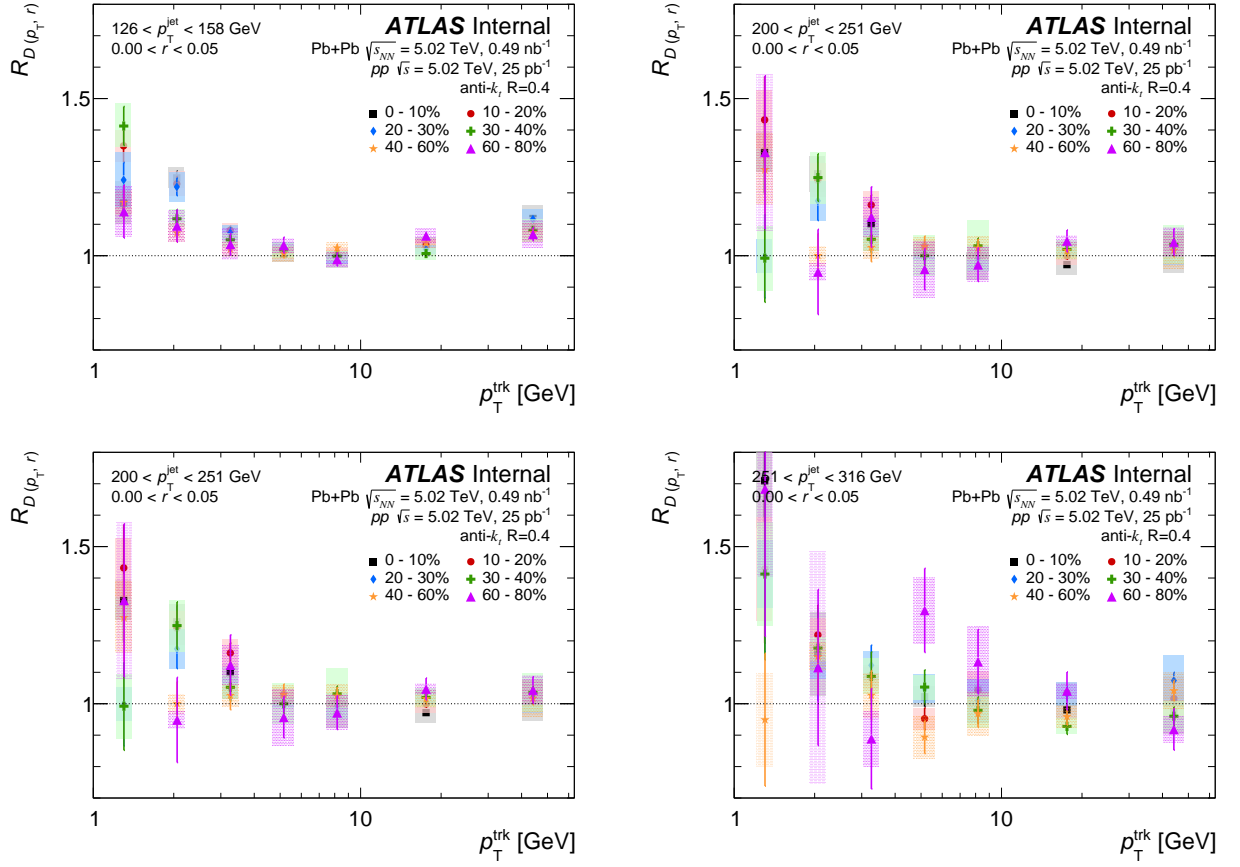
Figure 9: $R_{D(p_{\mathrm{T}},r)}$ for central Pb+Pb collisions as a function of p_{T} for different jet selections. The different colors represent different centrality bins. The vertical bars on the data points indicate statistical uncertainties while the shaded boxes indicate systematic uncertainties. The widths of the boxes are not indicative of the bin size and the points are shifted horizontally for better visibility.

358 Figure ?? shows the number density of extra particles with $p_{\mathrm{T}} < 4$ GeV as a function of distance from the
359 jet axis for different $p_{\mathrm{T}}^{\mathrm{jet}}$ ranges. It can be seen that the excess increases with increasing $p_{\mathrm{T}}^{\mathrm{jet}}$.

360 Figure ?? shows the number density of extra particles with $p_{\mathrm{T}} < 4$ GeV as a function of cumulative distance
361 from the jet axis for different $p_{\mathrm{T}}^{\mathrm{jet}}$ ranges. It can be seen that at large distances from the jet axis, the overall
362 change in low p_{T} particle density in Pb+Pb is greater by about 0.5 particles per unit area.

363 Figure ?? shows the modification between pp and Pb+Pb to the number of particles with $p_{\mathrm{T}} < 4$ GeV as a
364 function of distance from the jet axis for different $p_{\mathrm{T}}^{\mathrm{jet}}$ ranges. The maximal modification near the jet edge
365 at $0.4 < r < 0.5$ indicative of extra particles in that region that can come from large angle radiation.

366 Figure ?? shows the modification between pp and Pb+Pb to the number of particles with $p_{\mathrm{T}} < 4$ GeV as a
367 function of cumulative distance from the jet axis for different $p_{\mathrm{T}}^{\mathrm{jet}}$ ranges. There is an enhancement in the
368 number of particles for larger cones sizes
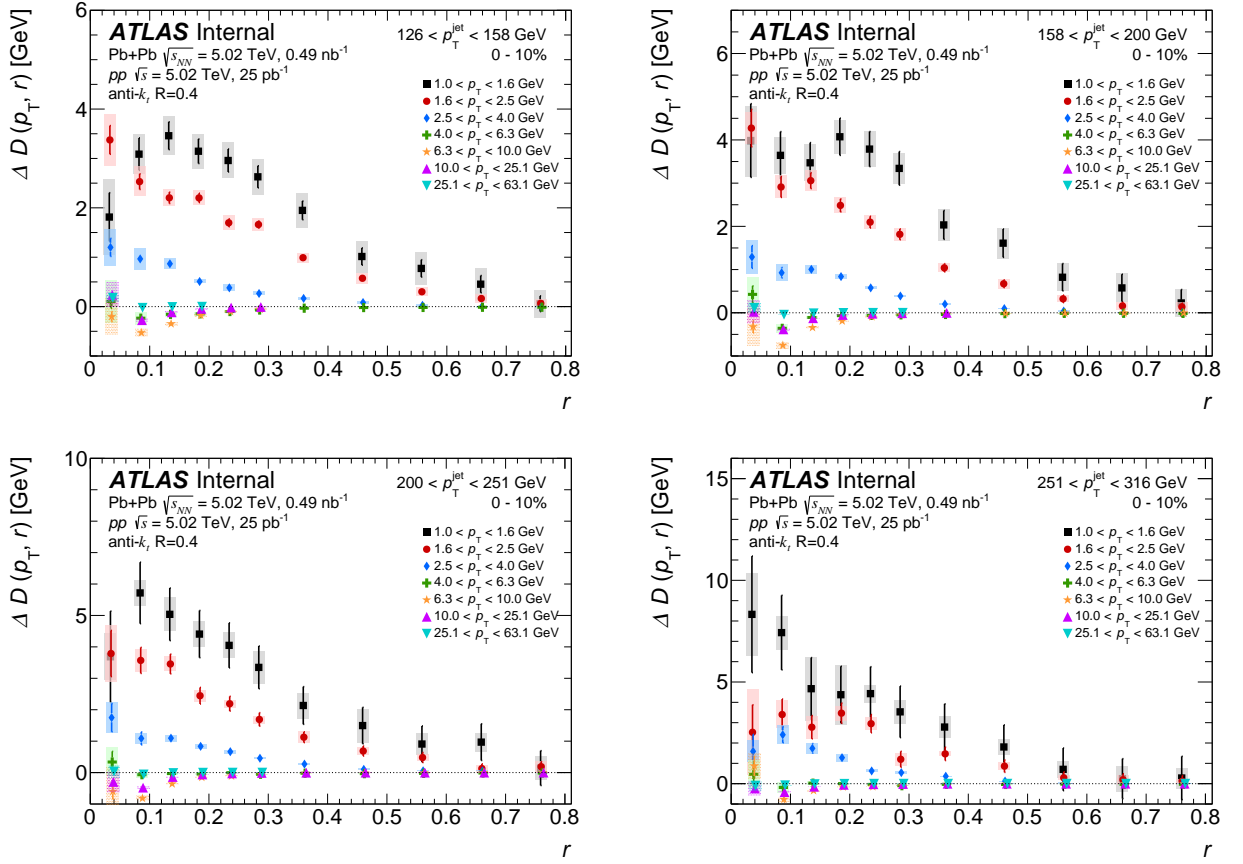
Figure 10: $\Delta D(p_T, r)$ as a function of r in central collisions for all p_T ranges in four p_T^{jet} selections: 126–158 GeV, 158–200 GeV, 200–251 GeV, and 251–316 GeV. The vertical bars on the data points indicate statistical uncertainties while the shaded boxes indicate systematic uncertainties. The widths of the boxes are not indicative of the bin size and the points are shifted horizontally for better visibility.

Delta D Low pT integral: See Figure **??**

$$\Delta_\Theta = \int_1^4 D(p_T)_{PbPb} - D(p_T)_{pp} dp_T \tag{12}$$

369

370 The measured dependence of $R_{D(p_T, r)}$ suggests that the energy lost by jets through the jet quenching
371 process is being transferred to particles with $p_T < 4.0$ GeV at larger radial distances from the jet axis. This
372 is qualitatively consistent with theoretical calculations [18, 19].

373 These observations are in agreement with the previous measurement of jet fragmentation functions [13–15,
374 17] and may indicate the dependence of the response of the hot dense matter to the momentum of a jet
375 passing through it.
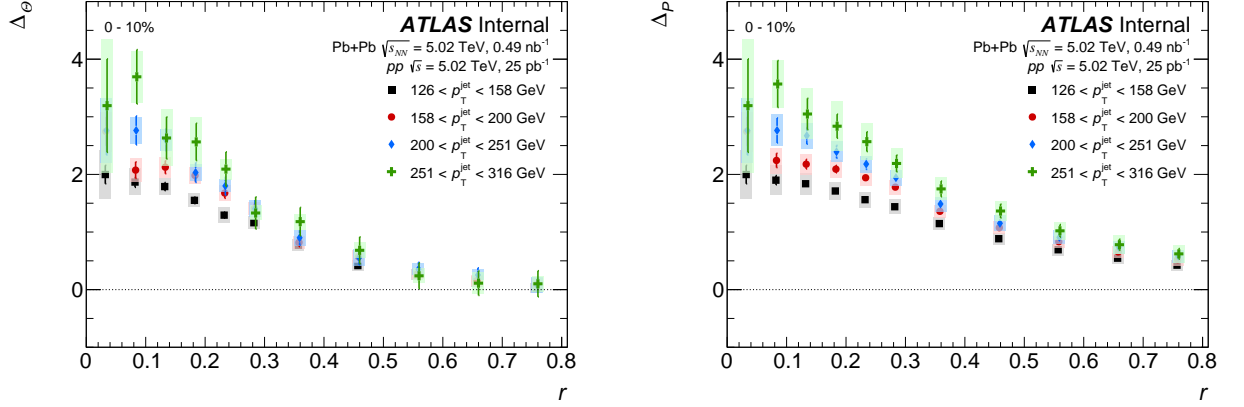
Figure 11: Δ_Θ (left) and Δ_P (right) as a function of r in central collisions for charged-particles with $p_T < 4$ GeV ranges in four p_T^{jet} selections: 126–158 GeV, 158–200 GeV, 200–251 GeV, and 251–316 GeV. The vertical bars on the data points indicate statistical uncertainties while the shaded boxes indicate systematic uncertainties. The widths of the boxes are not indicative of the bin size and the points are shifted horizontally for better visibility.
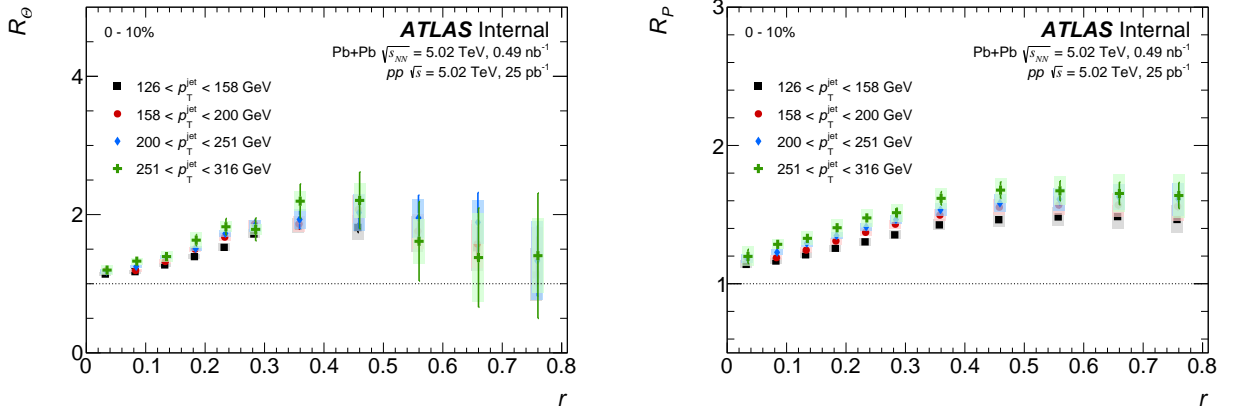
Figure 12: R_Θ (left) and R_P (right) as a function of r in central collisions for charged-particles with $p_T < 4$ GeV ranges in four p_T^{jet} selections: 126–158 GeV, 158–200 GeV, 200–251 GeV, and 251–316 GeV. The vertical bars on the data points indicate statistical uncertainties while the shaded boxes indicate systematic uncertainties. The widths of the boxes are not indicative of the bin size and the points are shifted horizontally for better visibility.

9 Summary

This paper presents a measurement of the yields of charged particle distributions, $D(p_T, r)$, inside and around $R = 0.4$ anti-k_t jets with $|y^{jet}|$ <1.7 up to a distance of $r = 0.8$ from the jet axis. The yields are measured in intervals of p_T^{jet} from 126 to 316 GeV in Pb+Pb and pp collisions at 5.02 TeV as a function of charged particle p_T and the angular distance r between the jet axis and charged particle.

Centrality dependent modifications to the yields, when compared to those measured in pp collisions, are observed. The magnitude of these modifications increases with increasing collision centrality. The $R_{D(p_T, r)}$ distributions for charged particles with $p_T < 4$ GeV are above unity and grow with increasing angular separation up to $r \sim 0.3$, showing weak to no dependence on r in the interval $0.3 < r < 0.6$ followed with a small decrease in the enhancement for $0.6 < r < 0.8$. For charged particles with $p_T > 4$ GeV, a suppression in $R_{D(p_T, r)}$ is observed, and the distributions decrease with increasing r for $r < 0.3$, with no r dependence for $r > 0.3$. These results show a broadening of the $D(p_T, r)$ distribution for low p_T particles inside the jet in central Pb+Pb collisions compared to those in pp collisions while for higher p_T particles angular distributions are narrower in Pb+Pb collisions compared to pp collisions. For all charged-particle p_T values the $R_{D(p_T, r)}$ values are greater than or equal to unity for small r values (inside the core of the jet). Between $0.1 < r < 0.25$, a statistically significant trend of increasing $R_{D(p_T, r)}$ with increasing p_T^{jet} is observed for low-p_T particles. No significant p_T^{jet} dependence is seen for particles with $p_T > 4$ GeV.

These measurements provide insight into the differential distributions of charged particles within jets as compared to the inclusive measurement of jet fragmentation functions. They provide new information about our understanding of the physics of soft gluon radiation and the response of the QGP to jets.

Acknowledgements

416 The crucial computing support from all WLCG partners is acknowledged gratefully, in particular from
417 CERN, the ATLAS Tier-1 facilities at TRIUMF (Canada), NDGF (Denmark, Norway, Sweden), CC-IN2P3
418 (France), KIT/GridKA (Germany), INFN-CNAF (Italy), NL-T1 (Netherlands), PIC (Spain), ASGC
419 (Taiwan), RAL (UK) and BNL (USA), the Tier-2 facilities worldwide and large non-WLCG resource
420 providers. Major contributors of computing resources are listed in Ref. [45].

421 In a paper, an appendix is used for technical details that would otherwise disturb the flow of the paper.
422 Such an appendix should be printed before the Bibliography.

References

424 [1] G. Roland, K. Šafařík and P. Steinberg, *Heavy-ion collisions at the LHC*, Prog. Part. Nucl. Phys. **77**
425 (2014) 70 (cit. on p. 2).

426 [2] W. Busza, K. Rajagopal and W. van der Schee, *Heavy Ion Collisions: The Big Picture, and the Big*
427 *Questions*, (2018), arXiv: 1802.04801 [hep-ph] (cit. on p. 2).

428 [3] ALICE Collaboration, *Measurement of charged jet suppression in Pb-Pb collisions at* $\sqrt{s_{NN}}$ = 2.76
429 *TeV*, JHEP **03** (2014) 013, arXiv: 1311.0633 [nucl-ex] (cit. on p. 2).

430 [4] ATLAS Collaboration, *Measurements of the Nuclear Modification Factor for Jets in Pb+Pb*
431 *Collisions at* $\sqrt{s_{\mathrm{NN}}}$ = 2.76 *TeV with the ATLAS Detector*, Phys. Rev. Lett. **114** (2015) 072302, arXiv:
432 1411.2357 [hep-ex] (cit. on p. 2).

433 [5] CMS Collaboration, *Measurement of inclusive jet cross sections in pp and PbPb collisions at*
434 $\sqrt{s_{NN}}$ = 2.76 *TeV*, Phys. Rev. C **96** (2017) 015202, arXiv: 1609.05383 [nucl-ex] (cit. on p. 2).

435 [6] ATLAS Collaboration, *Measurement of the nuclear modification factor for inclusive jets in Pb+Pb*
436 *collisions at* $\sqrt{s_{\mathrm{NN}}}$ = 5.02 *TeV with the ATLAS detector*, Phys. Lett. **B790** (2019) 108, arXiv:
437 1805.05635 [nucl-ex] (cit. on pp. 2, 5).

438 [7] ATLAS Collaboration, *Observation of a Centrality-Dependent Dijet Asymmetry in Lead-Lead*
439 *Collisions at* $\sqrt{s_{NN}}$ = 2.76 *TeV with the ATLAS Detector at the LHC*, Phys. Rev. Lett. **105**
440 (2010) 252303, arXiv: 1011.6182 [hep-ex] (cit. on p. 2).

441 [8] CMS Collaboration, *Observation and studies of jet quenching in PbPb collisions at nucleon-nucleon*
442 *center-of-mass energy = 2.76 TeV*, Phys. Rev. C **84** (2011) 024906, arXiv: 1102.1957 [nucl-ex]
443 (cit. on p. 2).

444 [9] ATLAS Collaboration, *Measurement of jet* p_{T} *correlations in Pb+Pb and pp collisions at* $\sqrt{s_{\mathrm{NN}}}$ =
445 *2.76 TeV with the ATLAS detector*, Phys. Lett. **B 774** (2017) 379, arXiv: 1706.09363 [hep-ex]
446 (cit. on pp. 2, 10).

447 [10] CMS Collaboration, *Studies of jet quenching using isolated-photon+jet correlations in PbPb and*
448 *pp collisions at* $\sqrt{s_{NN}}$ = 2.76 *TeV*, Phys. Lett. **B 718** (2013) 773, arXiv: 1205.0206 [nucl-ex]
449 (cit. on p. 2).

450 [11] CMS Collaboration, *Modification of jet shapes in PbPb collisions at* $\sqrt{s_{NN}}$ = 2.76 *TeV*, Phys. Lett.
451 **B 730** (2014) 243, arXiv: 1310.0878 [nucl-ex] (cit. on p. 2).

452 [12] ATLAS Collaboration, *Measurement of inclusive jet charged-particle fragmentation functions in*
453 *Pb+Pb collisions at* $\sqrt{s_{NN}}$ = 2.76 *TeV with the ATLAS detector*, Phys. Lett. B **739** (2014) 320,
454 arXiv: 1406.2979 [hep-ex] (cit. on p. 2).

[13] CMS Collaboration, *Measurement of jet fragmentation in PbPb and pp collisions at* $\sqrt{s_{NN}}$ = 2.76 *TeV*, Phys. Rev. C **90** (2014) 024908, arXiv: 1406.0932 [nucl-ex] (cit. on pp. 2, 19).

[14] ATLAS Collaboration, *Measurement of jet fragmentation in Pb+Pb and pp collisions at* $\sqrt{s_{NN}}$ = 2.76 *TeV with the ATLAS detector at the LHC*, Eur. Phys. J. C **77** (2017) 379, arXiv: 1702.00674 [hep-ex] (cit. on pp. 2, 9, 19).

[15] ATLAS Collaboration, *Measurement of jet fragmentation in Pb+Pb and pp collisions at* $\sqrt{s_{NN}}$ = 5.02 *TeV with the ATLAS detector*, Phys. Rev. **C98** (2018) 024908, arXiv: 1805.05424 [nucl-ex] (cit. on pp. 2, 6, 9, 10, 19).

[16] CMS Collaboration, *Decomposing transverse momentum balance contributions for quenched jets in PbPb collisions at* $\sqrt{s_{NN}}$ = 2.76 *TeV*, JHEP **11** (2016) 055, arXiv: 1609.02466 [nucl-ex] (cit. on p. 2).

[17] CMS collaboration, *Jet properties in PbPb and pp collisions at* $\sqrt{s_{NN}}$ = 5.02 *TeV*, JHEP **05** (2018) 006, arXiv: 1803.00042 [nucl-ex] (cit. on pp. 2, 19).

[18] G.-Y. Qin and X.-N. Wang, *Jet quenching in high-energy heavy-ion collisions*, Int. J. Mod. Phys. E **24** (2015) 1530014, arXiv: 1511.00790 [hep-ph] (cit. on pp. 2, 19).

[19] J.-P. Blaizot, Y. Mehtar-Tani and M. A. C. Torres, *Angular structure of the in-medium QCD cascade*, Phys. Rev. Lett. **114** (2015) 222002, arXiv: 1407.0326 [hep-ph] (cit. on pp. 2, 19).

[20] M. Cacciari, G. P. Salam and G. Soyez, *The Anti-k(t) jet clustering algorithm*, JHEP **0804** (2008) 063, arXiv: 0802.1189 [hep-ph] (cit. on p. 3).

[21] ATLAS Collaboration, *The ATLAS Experiment at the CERN Large Hadron Collider*, JINST **3** (2008) S08003 (cit. on pp. 3, 4).

[22] ATLAS Collaboration, *ATLAS Insertable B-Layer Technical Design Report*, (2010), ATLAS-TDR-19, URL: http://cds.cern.ch/record/1291633 (cit. on p. 4).

[23] ATLAS Collaboration, *ATLAS Insertable B-Layer Technical Design Report Addendum*, (2012), ATLAS-TDR-19-ADD-1, URL: http://cds.cern.ch/record/1451888 (cit. on p. 4).

[24] ATLAS Collaboration, *Measurement of longitudinal flow de-correlations in Pb+Pb collisions at* $\sqrt{s_{NN}}$ = 2.76 *and 5.02 TeV with the ATLAS detector*, Eur. Phys. J. C **78** (2018) 142, arXiv: 1709.02301 [nucl-ex] (cit. on p. 4).

[25] P. Nason, *A New method for combining NLO QCD with shower Monte Carlo algorithms*, JHEP **11** (2004) 040, arXiv: hep-ph/0409146 [hep-ph] (cit. on p. 4).

[26] T. Sjöstrand et al., *An Introduction to PYTHIA 8.2*, Comput. Phys. Commun. **191** (2015) 159, arXiv: 1410.3012 [hep-ph] (cit. on p. 4).

[27] ATLAS Collaboration, *ATLAS Run 1 Pythia8 tunes*, (2014), ATLAS-PHYS-PUB-2014-021, URL: https://cds.cern.ch/record/1966419 (cit. on p. 4).

[28] R. D. Ball et al., *Parton distributions with LHC data*, Nucl. Phys. B **867** (2013) 244, arXiv: 1207.1303 [hep-ph] (cit. on p. 4).

[29] GEANT4 Collaboration, S. Agostinelli et al., *GEANT4: A simulation toolkit*, Nucl. Instrum. Meth. A **506** (2003) 250 (cit. on p. 5).

[30] ATLAS Collaboration, *The ATLAS Simulation Infrastructure*, Eur. Phys. J. C **70** (2010) 823, arXiv: 1005.4568 [physics.ins-det] (cit. on p. 5).

[31] ATLAS Collaboration, *Measurement of the azimuthal anisotropy for charged particle production in* $\sqrt{s_{NN}}$ = 2.76 *TeV lead-lead collisions with the ATLAS detector*, Phys. Rev. C **86** (2012) 014907, arXiv: 1203.3087 [hep-ex] (cit. on pp. 5, 6).

[32] ATLAS Collaboration, *Jet energy scale measurements and their systematic uncertainties in proton-proton collisions at* $\sqrt{s}$ = 13 *TeV with the ATLAS detector*, Phys. Rev. **D 96** (2017) 072002, arXiv: 1703.09665 [hep-ex] (cit. on pp. 5, 8).

[33] ATLAS Collaboration, *Properties of jets and inputs to jet reconstruction and calibration with the ATLAS detector using proton–proton collisions at* $\sqrt{s}$ = 13 *TeV*, ATL-PHYS-PUB-2015-036, 2015, URL: https://cds.cern.ch/record/2044564 (cit. on p. 5).

[34] M. Aaboud et al., *Measurement of photon-jet transverse momentum correlations in 5.02 TeV Pb+Pb and pp collisions with ATLAS*, Phys. Lett. **B 789** (2019) 167, arXiv: 1809.07280 [nucl-ex] (cit. on p. 5).

[35] ATLAS Collaboration, *Performance of the ATLAS Track Reconstruction Algorithms in Dense Environments in LHC Run 2*, Eur. Phys. J. **C 77** (2017) 673, arXiv: 1704.07983 [hep-ex] (cit. on p. 5).

[36] G. D'Agostini, *A Multidimensional unfolding method based on Bayes' theorem*, Nucl. Instrum. Meth. A **362** (1995) 487 (cit. on p. 7).

[37] T. Adye, *Unfolding algorithms and tests using RooUnfold*, Proceedings of the PHYSTAT 2009 Workshop, CERN, Geneva, Switzerland, CERN-2011-006, pp 313 (2011), arXiv: 1105.1160 [physics.data-an] (cit. on p. 7).

[38] ATLAS Collaboration, *Jet energy measurement with the ATLAS detector in proton-proton collisions at* $\sqrt{s}$ = 7 *TeV*, Eur. Phys. J. C **73** (2013) 2304, arXiv: 1112.6426 [hep-ex] (cit. on pp. 7, 8).

[39] ATLAS Collaboration, *Jet energy scale and its uncertainty for jets reconstructed using the ATLAS heavy ion jet algorithm*, (), ATLAS-CONF-2015-016, URL: https://cds.cern.ch/record/2008677 (cit. on p. 8).

[40] ATLAS Collaboration, *Jet energy measurement and its systematic uncertainty in proton-proton collisions at* $\sqrt{s}$ = 7 *TeV with the ATLAS detector*, Eur. Phys. J. C **75** (2015) 17, arXiv: 1406.0076 [hep-ex] (cit. on p. 8).

[41] ATLAS Collaboration, *Jet energy resolution in proton-proton collisions at* $\sqrt{s}$ = 7 *TeV recorded in 2010 with the ATLAS detector*, Eur. Phys. J. C **73** (2013) 2306, arXiv: 1210.6210 [hep-ex] (cit. on p. 9).

[42] ATLAS Collaboration, *Data-driven determination of the energy scale and resolution of jets reconstructed in the ATLAS calorimeters using dijet and multijet events at* $\sqrt{s}$ = 8 *TeV*, (2015), ATLAS-CONF-2015-017, URL: https://cds.cern.ch/record/2008678 (cit. on p. 9).

[43] ATLAS Collaboration, *Early Inner Detector Tracking Performance in the 2015 Data at* $\sqrt{s}$ = 13 *TeV*, ATL-PHYS-PUB-2015-051, 2015, URL: https://cds.cern.ch/record/2110140 (cit. on p. 9).

[44] ATLAS Collaboration, *Measurement of track reconstruction inefficiencies in the core of jets via pixel dE/dx with the ATLAS experiment using* $\sqrt{s}$ = 13 *TeV pp collision data*, ATL-PHYS-PUB-2016-007, 2016, URL: https://cds.cern.ch/record/2140460 (cit. on p. 9).

[45] ATLAS Collaboration, *ATLAS Computing Acknowledgements*, ATL-GEN-PUB-2016-002, URL: https://cds.cern.ch/record/2202407 (cit. on p. 21).

Auxiliary material

In an ATLAS paper, auxiliary plots and tables that are supposed to be made public should be collected in an appendix that has the title 'Auxiliary material'. This information will appear on the public webpage, but will not be included in the document submitted to arXiv and to the journal.
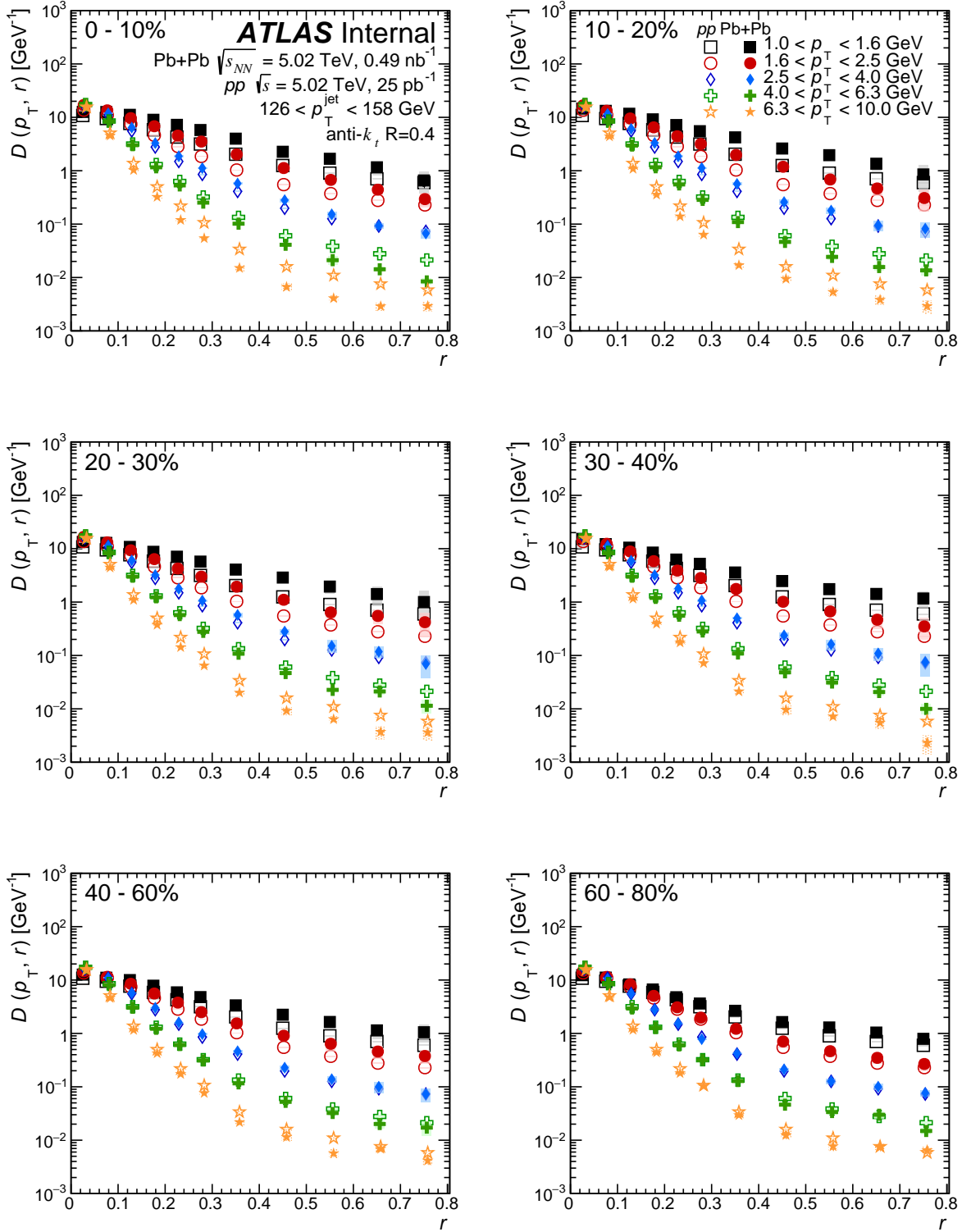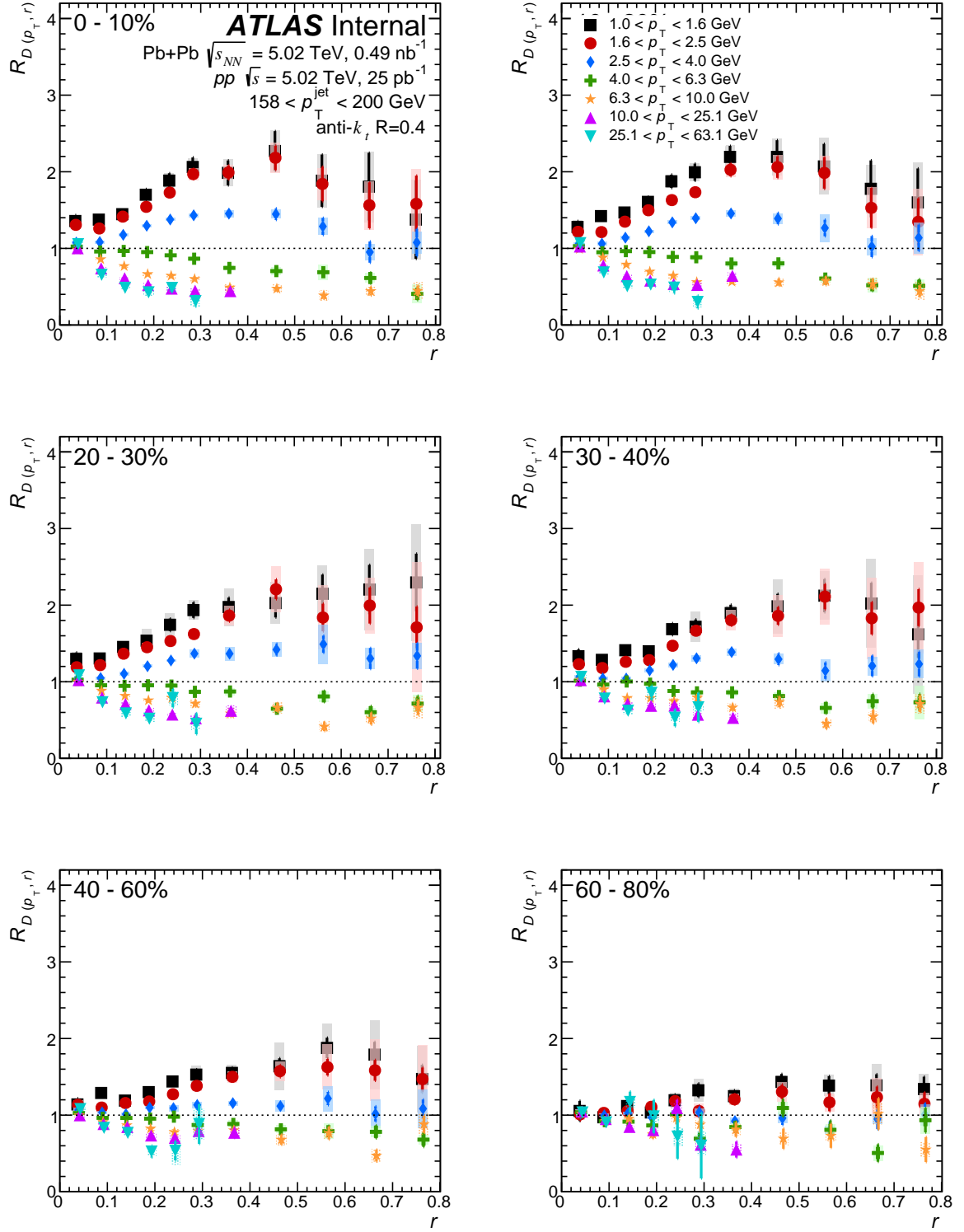
Figure 13: Full set of $D(p_T, r)$ distributions for 126–158 GeV jets.
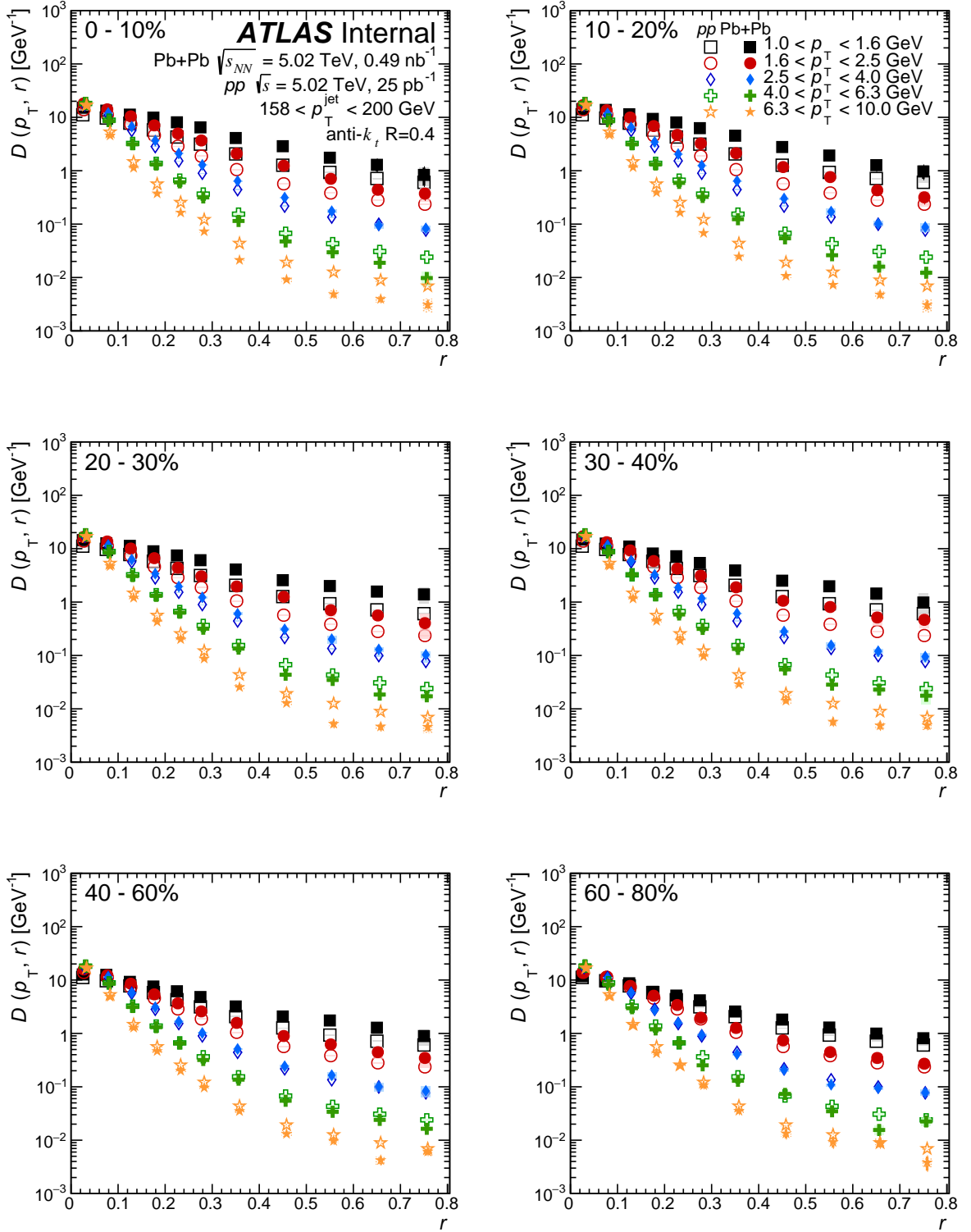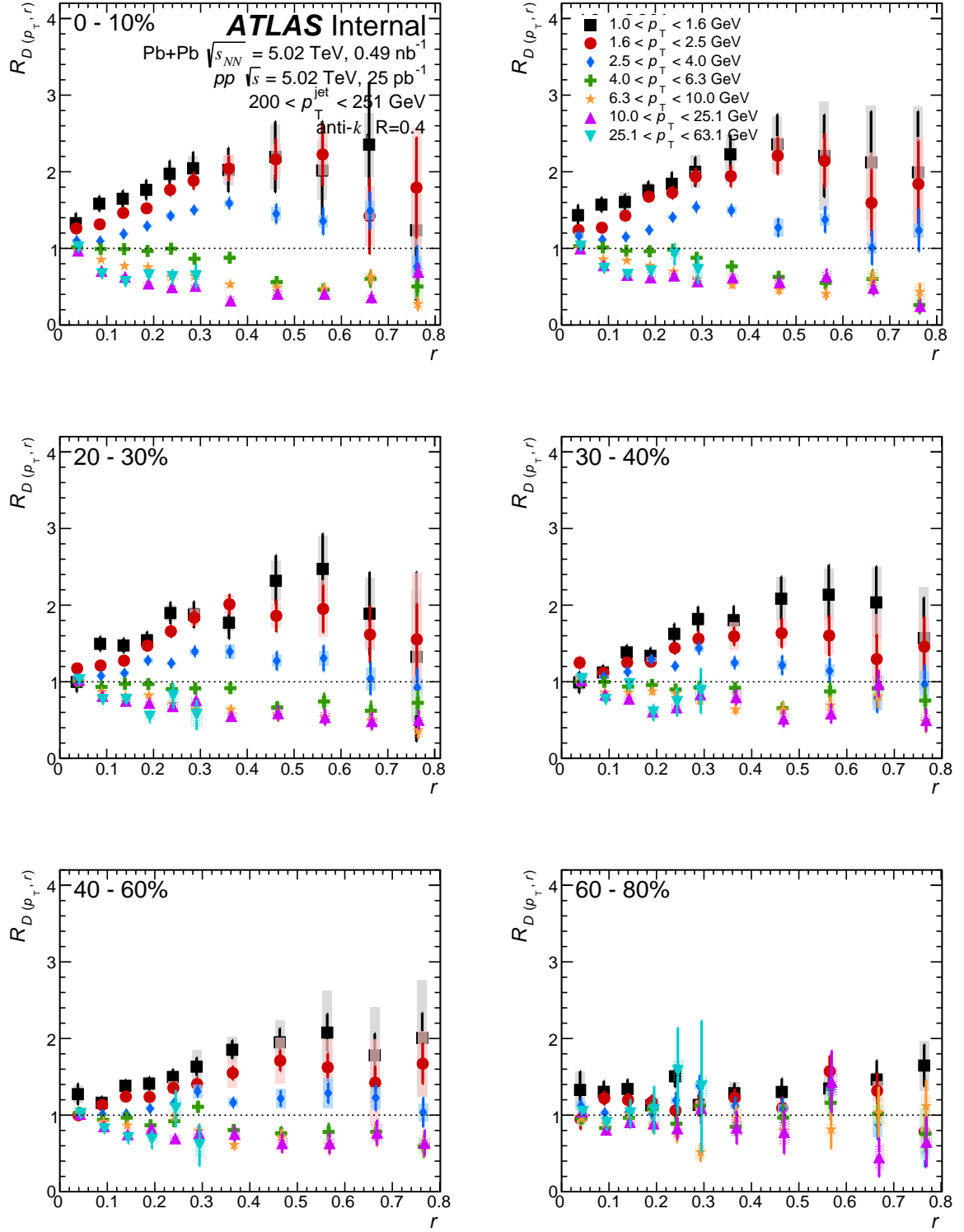
Figure 14: Full set of $D(p_T, r)$ distributions for 158–200 GeV jets.
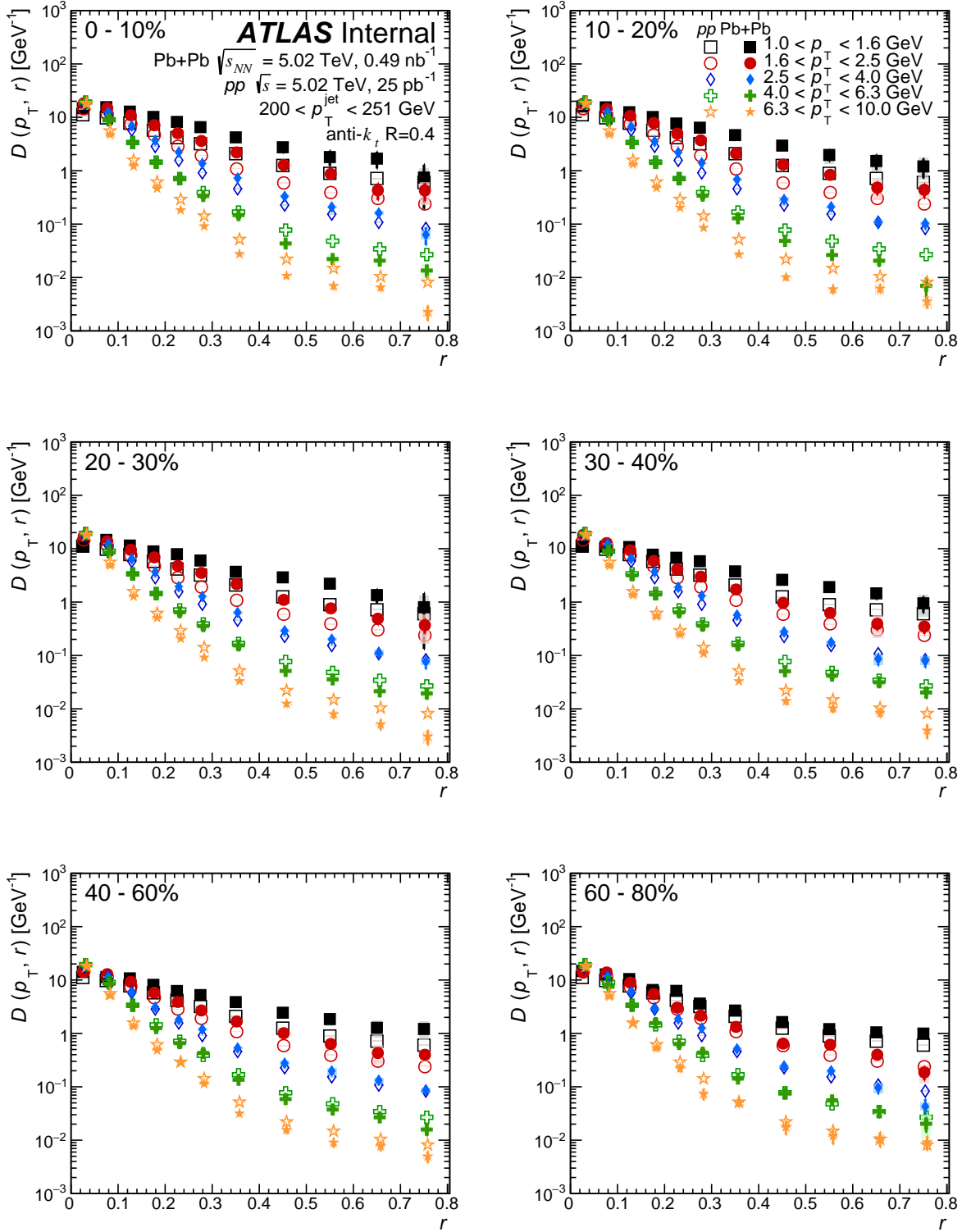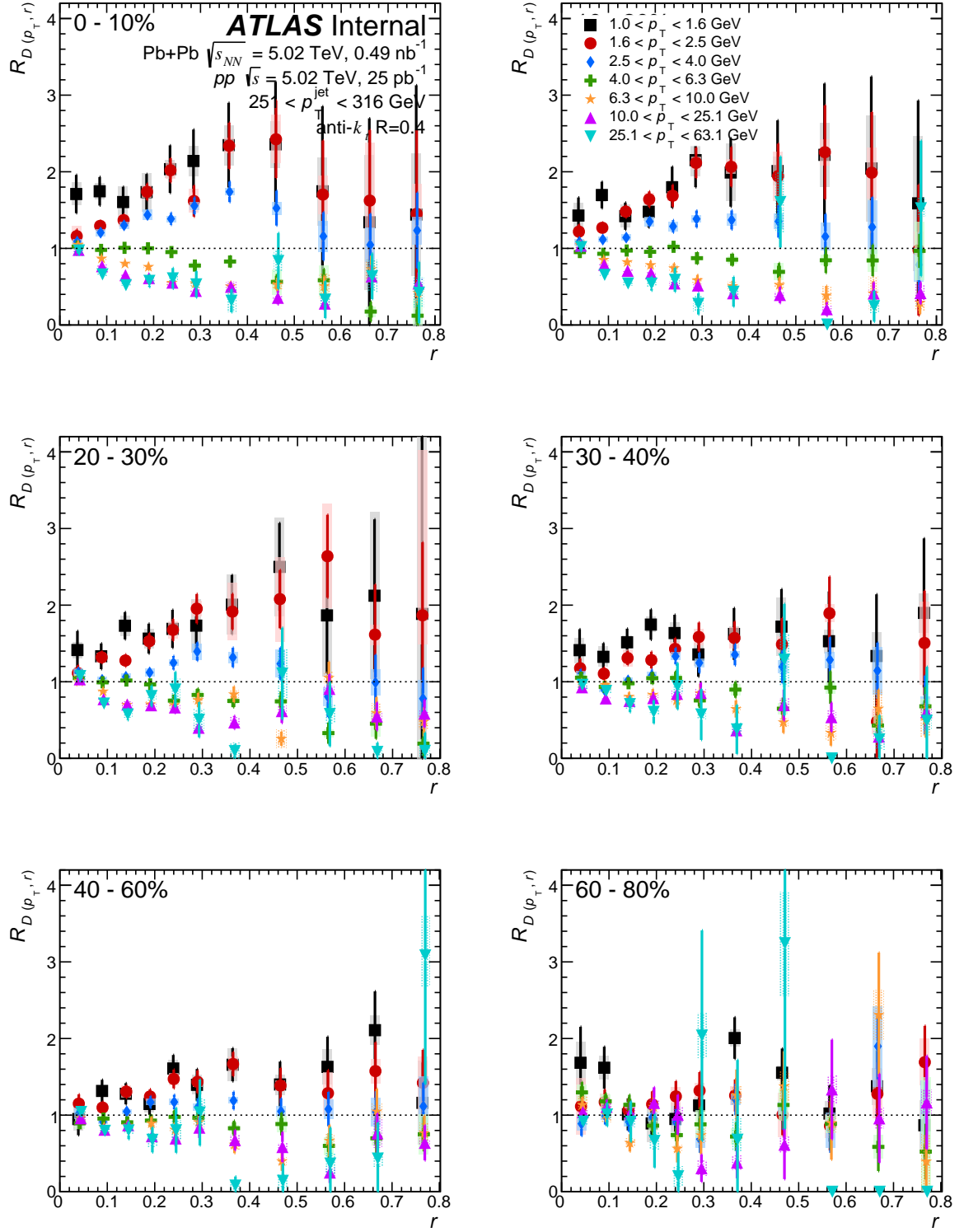
Figure 15: Full set of $D(p_T, r)$ distributions for 200–251 GeV jets.
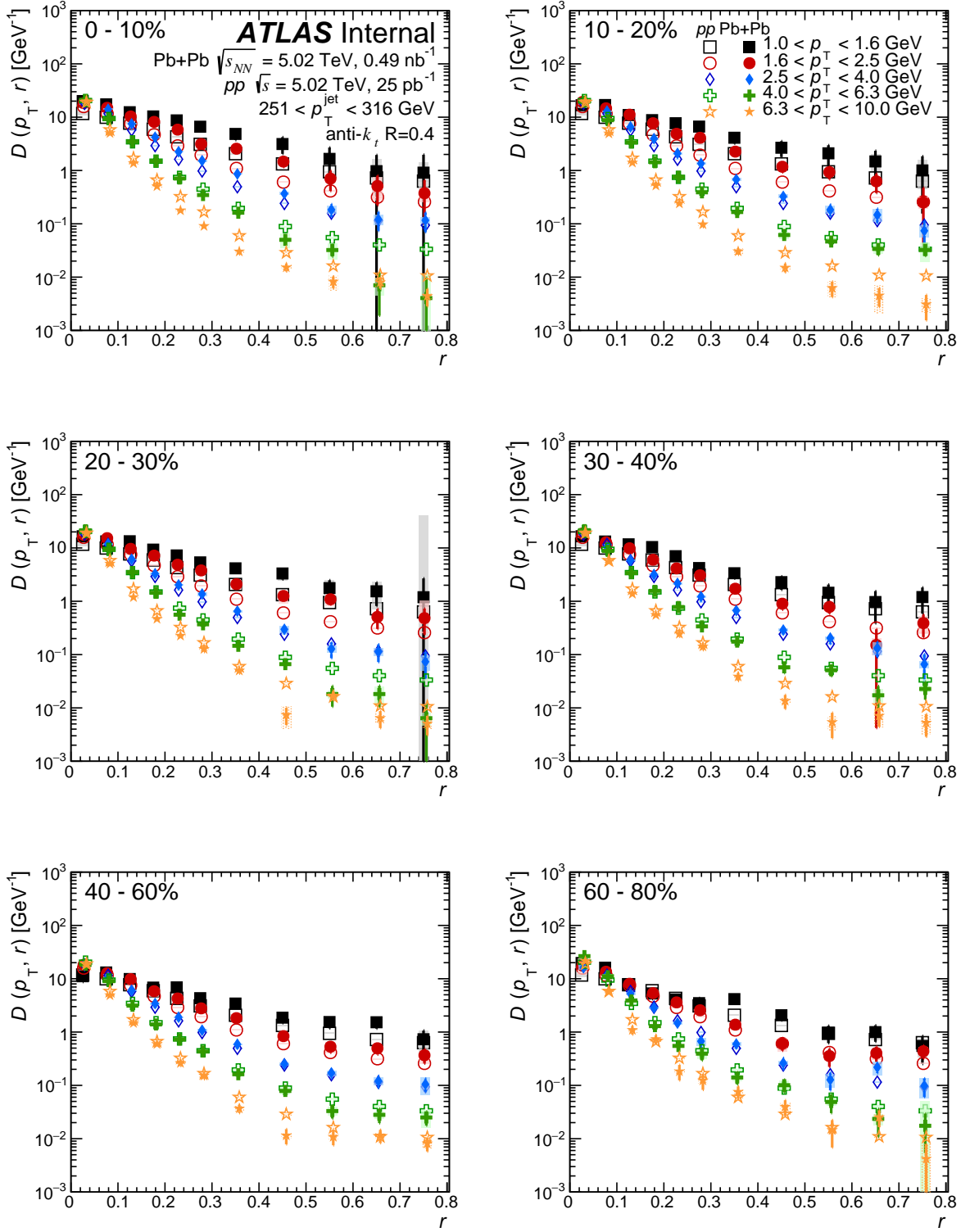
Figure 16: Full set of $D(p_T, r)$ distributions for 251–316 GeV jets.
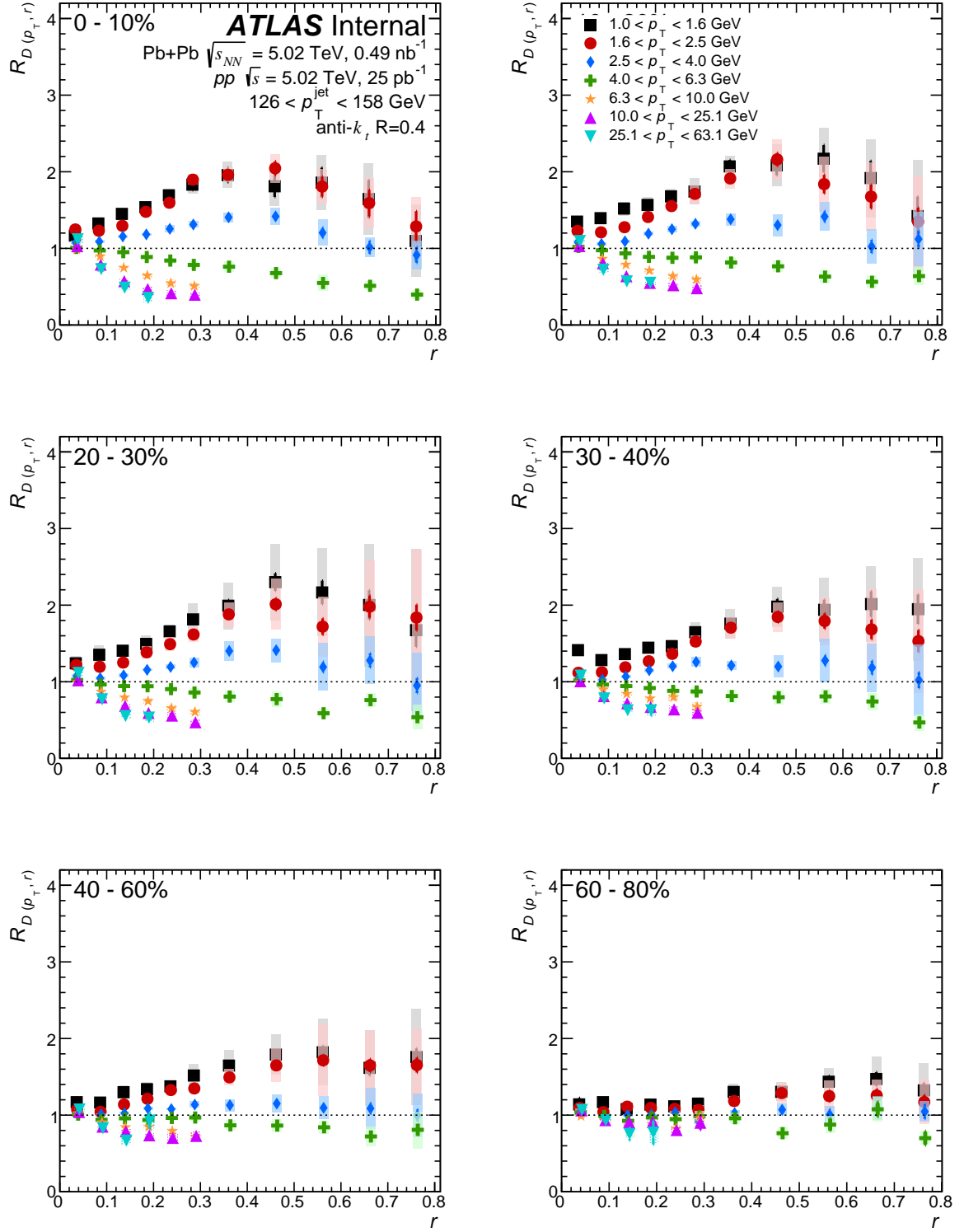
Figure 17: Full set of $R_{D(p_T,r)}$ distributions for 126–158 GeV jets.

Figure 18: Full set of $R_{D(p_T,r)}$ distributions for 158–200 GeV jets.

Figure 19: Full set of $R_{D(p_{\mathrm{T}},r)}$ distributions for 200–251 GeV jets.

Figure 20: Full set of $R_{D(p_T,r)}$ distributions for 251–316 GeV jets.